Chapter 6. An experimental and numerical study for Mode I fracture parameter characterization of a cracked giant magnetostrictive material

6.1. Introduction

Giant magnetostrictive materials, in particular Terfenol-D, have attractive properties such as high saturation magnetostriction, variable elastic modulus, high curie temperature, and faster response to operational factors, and thus have potential applications in sensors, actuators, acoustic transducers, stress monitoring devices, linear motors, micro-pumps, and micro-positioning [1–3] [4,5]. These unique features make them the most sought-after intelligent materials for modern applications in the automotive, avionics, construction engineering, micro-magneto-mechanical systems, healthcare, and industrial automation sectors [1,3,9,10].

However, the attractiveness comes with a cost, that the Terfenol-D is an expensive alloy and challenging to manufacture owing to the high reactivity of its constituent elements and impurities [18,19]. The biggest drawback of Terfenol-D is its extremely brittle characteristics, and in the presence of manufacturing flaws or cracks, it has a substantially lower tensile strength (25-50 MPa) than its compressive strength [14,18,20,28]. The failure and fracture pattern which might be considered stochastic in nature to predict with certainty can therefore compromise its performance and expose it to in-service failures. These constraints encourage researchers to dig further into the subject of defect susceptibility in Terfenol-D. Significant efforts have been made to investigate the influence of crack and notches on the tensile behaviour of the brittle materials and in past decades [21–23]. From the literature studies, it was apparent that experimental and numerical stochastic works are a few for such coupled magnetic and stress-dependent elasticity fracture studies of giant magnetostrictive materials such as Terfenol-D. Consequently, extensive research has also been carried out concerning the performance of the giant magnetostrictive materials, but only a minimal effort has been dedicated to understand the fracture behaviour of such materials. This material is brittle enough to exhibit catastrophic fracture dominant failure behaviour without any precursor warning.

This chapter laid a three-dimensional procedure to accurately determine the in-service fracture strength of the Terfenol-D. It constitutes exclusive magneto-elastic flexure experiments on the three-point SENB specimens and finite element analyses to investigate the fracture parameters of the bi-nonlinear Terfenol-D. The magneto-elastic coupled field three-point bend experimentation on two sets of single edge notch bend (SENB) specimens of Terfenol-D is carried out in the presence and absence of the magnetic field as per ASTM standards. The digital image correlation technique is used to capture the load line and crack opening displacement variation with peak fracture load (P_{max}) data. The Terfenol-D's mean peak fracture load can be predicted with a weakest link theory based Weibull approach [29,30] by evaluating the Weibull parameters (specifically Weibull modules and Weibull characteristics strength) for enhancing the reliability of structures at extreme service conditions. The Weibull modulus and goodness of fit are assessed using linear regression analysis (LIN2), biased and unbiased maximum likelihood estimation (MLE2-B & MLE2-U) approach. A three-dimensional J-integral definition for characterizing the fracture behaviour has also been used as described in Chapter 4. , which is subsequently used to characterize the crack front singularity near the fracture process zone. Then, to compute the critical strain energy release rate of the Terfenol-D SENB specimen under an applied external magnetic field, finite element analyses employing a vector generalized nonlinear hysteretic magneto-thermo-elastic constitutive model as proposed in Chapter 3 [127] have been conducted. The calibrated material parameters from Chapter 5 have been employed in the finite element procedures. Critical strain energy release rate J_{Ic} was calculated using the mean peak fracture load in both absence and presence of the external magnetic field. Finally, the influence of bi-nonlinear modularity and applied external magnetic field on the fracture behaviour of the Terfenol-D SENB fracture specimen were compared with the unimodular experimental results and substantial differences were reported. The stipulation and importance of considering the bi-nonlinear critical strain energy release rate J_{Ic} in the context of a coupled magneto-elastic field was discussed certifying the observations.

6.2. Fracture toughness experiment

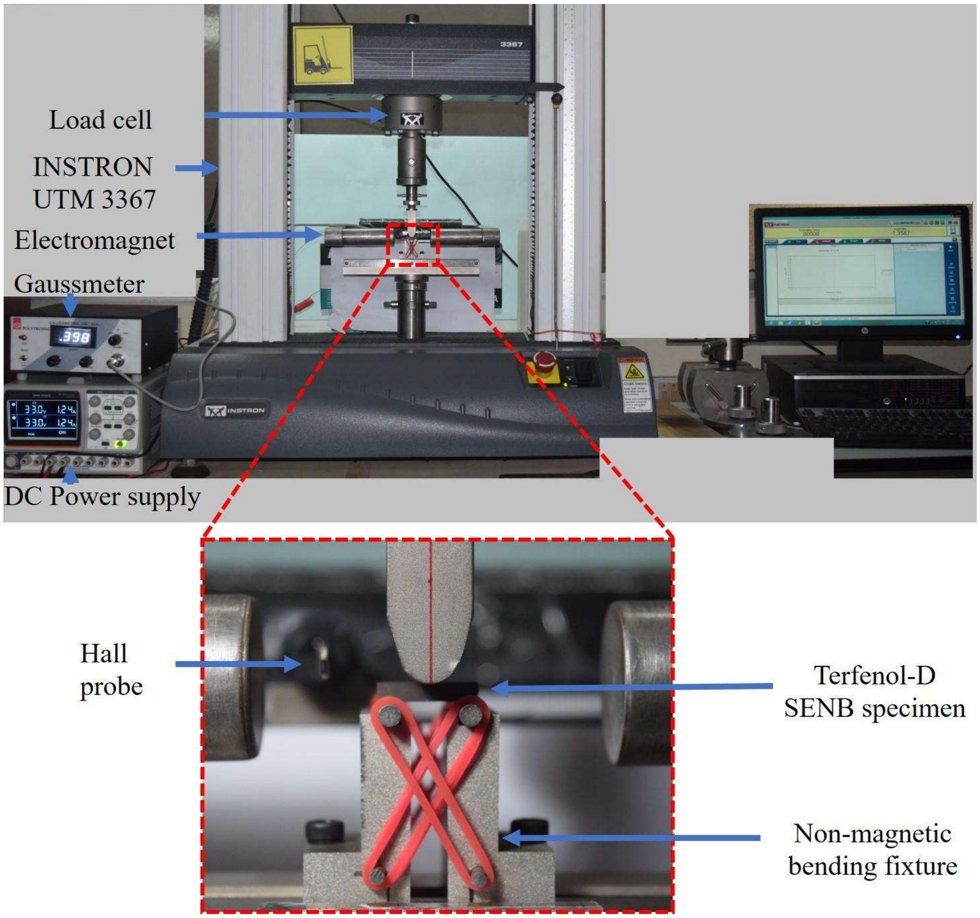

Figure 6.1 Experimental setup for fracture toughness test of single edge notch bend (SENB) specimen in three-point loading under magnetic field

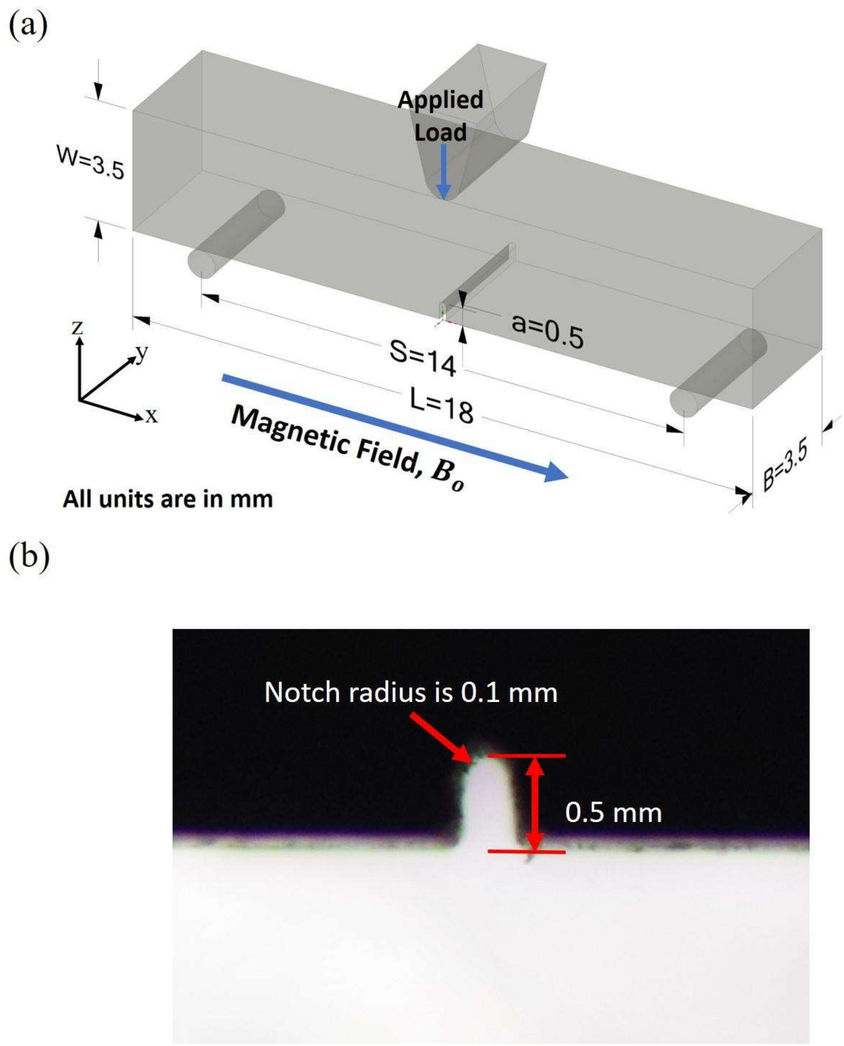

Figure 6.2 (a) Specimens geometry **(b)** Enlarged view of the notch edge as per ASTM standard

A three-point bend flexure test is performed to characterize the fracture parameters of giant magnetostrictive material (i.e., Terfenol-D) in the coupled magneto-elastic field, which is procured from Lanzhou Jian Xing Commercial and Trading Co., Ltd. in cuboid bar shapes with a cross-section of $3.5 \times 3.5\ \text{mm}^2$, respectively. Fracture toughness tests are performed on Terfenol-D SENB specimens under the externally applied magnetic fields in accordance with ASTM E399-20a [131] and E1820-18a [132], as shown in **Figure 6.1** and **Figure 6.2**. The impact of nonlinear elasticity and magnetic field on fracture properties have been investigated. For the test, bending fixtures made of the nonmagnetic steel grade 316 are used.

The bending fixtures are crafted so that when the specimen is loaded, the support rollers can roll and translate minimally, and the rollers are first put against stops that establish the span length using low tension rubg bands. Thirty cuboids of Terfenol-D having square cross-section ($3.5\ mm\ \times\ 3.5\ mm$) and length dimension 36 mm are used to prepare the SENB fracture specimens. From each cuboid, two fracture specimen are prepared: One to test with the presence of magnetic field and another without it for the characterization of fracture strength. Each specimen has a span length of 14 mm. Considering the high cost of the Terfenol-D material, the dimension and number of specimens are restricted to satisfy both the ASTM standard and Weibull model efficiently. Another challenge is the brittleness of the material to inscribe a notch in it. A high precision wire cut electro discharge machining (Expresscut Ex-4032C) is employed to produce a notch of 0.5 mm length and 0.1 mm tip radius (**Figure 6.2b**). Since most Terfenol-D transducers have magnetic operating regimes ranging between 0.02 T to 0.05 T, thus an electromagnet is used to apply a homogenous external magnetic field of magnetic induction ($B_o = 0.03\ T$) in the longitudinal direction of the specimen. Here, $B_0 = \mu_0 H$, is the magnetic induction produced in the air due to the applied magnetic field H, where $\mu_o = 4\pi \times 10^{-7}\ H/m$ is air/vacuum permeability. A load P is applied coaxially to the straight notch with a specific loading rate of 0.5 N/s to mimic the quasistatic conditions. The fracture test data (such as peak fracture load (P_{max}), load-line displacement and crack opening displacement) are collected utilising digitalized image correlation software and continuous image capturing with a high-speed camera set up attached to the 64-bit INSTRON UTM. All the mechanical tests are carried out with a resolution of 0.0001 N in the Bluehill 3 interface. The deformation measurement between two subsequent intervals of the increasing force is close to 5×10^{-5} mm, which demonstrates the measuring precision of the equipment.

6.3. Experimental evaluation of strain energy release rate J_{Ic}

The three-point bend SENB fracture specimens with the $S/W = 4$ and $a/W = 0.1428$ are tested, as per the ASTM E1820 standard. The cross-head speed for the flexure fracture testing has been kept very slow at 0.5 N/s, as the Terfenol-D is highly brittle. Aside from gathering a high number of data points for precisely calculating the critical strain energy J_{Ic}, the slow loading rate provides less vibration in the fracture propagation zone, protecting the specimen. As a result of a large number of data points collected and the load-displacement plot also exhibits a very smooth curve. The peak fracture load data is measured for each specimen. The peak fracture load for the cracked specimens of magnetostrictive Terfenol-D are then used to evaluate the experimental J_{Ic} values based on unimodular material model and bi-nonlinear material model in the following subsections.

6.3.1. For unimodular material

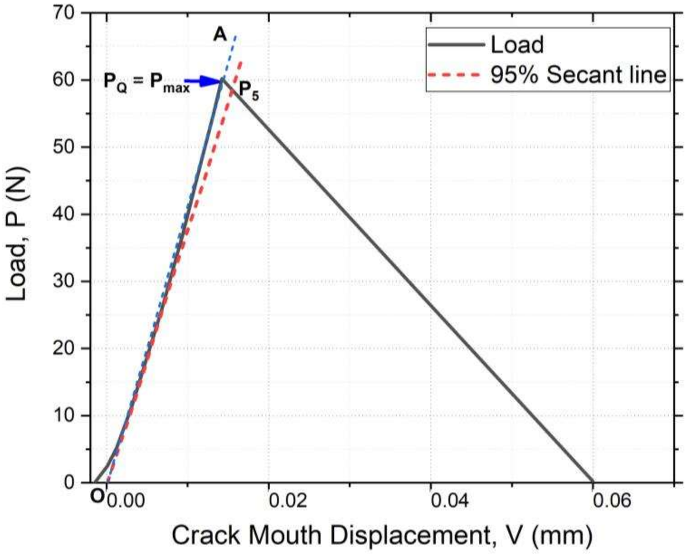

Figure 6.3 Force vs. crack mouth displacement curve for random Terfenol-D specimen

This subsection displays the method for evaluation of the conditional peak fracture load (P_Q), fracture toughness ($\boldsymbol{K_{Ic}}$) and J-Integral ($\boldsymbol{J_{Ic}}$) for a random sample data in magneto-elastic environment assuming Terfenol-D is an unimodular linear material. The critical fracture toughness parameter (K_{Ic}) for quasistatic three-point bending has been evaluated from the conditional force value P_Q recorded in the bending load and crack mouth opening displacement (CMOD) plot as per ASTM E399. P_Q is determined by plotting the secant line OP$_5$, as shown in **Figure 6.3**, which passes through the test record origin O and has a slope equal to the slope of the tangent OA to the first linear segment of the curve. In **Figure 6.3**, peak fracture load (P_{max}) preceding the P_5 which exceeds it, hence, P_{max} is equal to P_Q. The fracture toughness value for the conditional load P_Q is denoted by K_Q. Here, the ratio $P_{max}/P_Q = 1$, does not exceed 1.10 and the value $2.5\left(\frac{K_Q}{\sigma_{YS}}\right)^2$, where σ_{YS} is yield strength in tension, is less than the sample ligament size, $W - a$, thus K_Q will be equal to K_{Ic}. The fracture toughness K_{Ic} for the Terfenol-D sample can be calculated in Pa $\sqrt{\text{m}}$ as follows

$$K_{Ic} = K_Q = \frac{P_Q S}{B W^{\frac{3}{2}}} \cdot f\left(\frac{a}{W}\right) \tag{6.1}$$

where

$$f\left(\frac{a}{W}\right) = 3\sqrt{\frac{a}{W}} \cdot \frac{1.99 - \left(\frac{a}{W}\right)\left(1 - \frac{a}{W}\right)\left[2.15 - 3.93\frac{a}{W} + 2.7\left(\frac{a}{W}\right)^2\right]}{2\left(1 + 2\frac{a}{W}\right)\left(1 - \frac{a}{W}\right)^{\frac{3}{2}}}$$

for which 'a' is the crack size, 'B' is the width, 'W' is the thickness and 'S' is the span length of the Terfenol-D SENB specimen.

Here, it is worth noting that critical energy release rate value (G_{Ic}) is similar to the critical J-integral value (J_{Ic}) for the brittle material like Terfenol-D in which no plastic zone appears near the crack tip. To be consistent with the fracture parameters in numerical models, critical energy release rate value was also computed. According to ASTM E1820, the corresponding values of the critical J-integral (J_{Ic}) may be evaluated from the fracture toughness K_{Ic} using the following expression

$$J_{Ic} = \frac{K_{Ic}^2(1 - \nu^2)}{E_{in}} \tag{6.2}$$

where E_{in} is intrinsic Young's modulus, ν is Poisson's ratio.

6.3.2. For variable modulus material

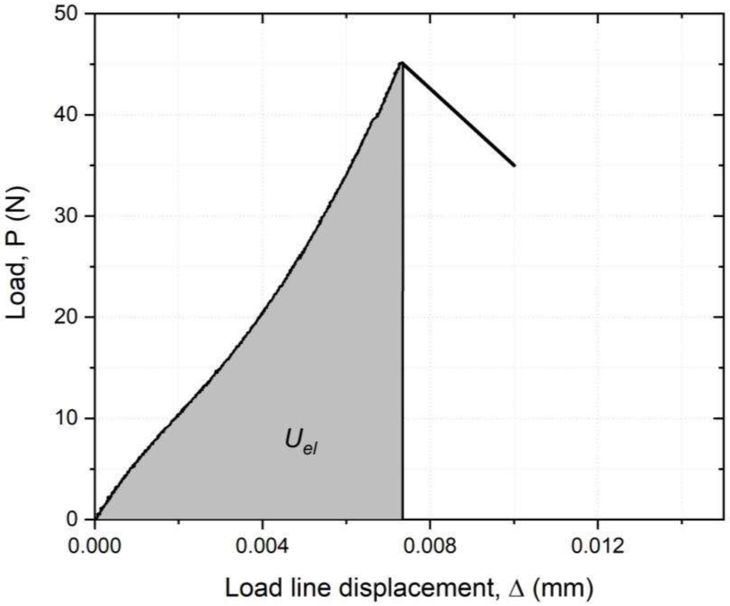

Figure 6.4 Load-displacement curves showing elastic component of absorbed energy U_{el}

Since the Terfenol-D possess the stress and magnetization dependent variable elasticity (ΔE effect), thus it is convenient to use J estimation methods based on the area under the load-displacement curve in determining the energy release rate values from test records. **Figure 6.4** shows the load-displacement plot for the random Terfenol-D SENB specimen in presence of magnetic field for evaluation of energy release rates. Sumpter and Turner [133,134] developed a more general relationship for calculating the J-integral as a sum of elastic and plastic components. The elastic component J_{el} can be written as:

$$J_{el} = \eta_{el} \frac{U_{el}}{B(W - a)} \tag{6.3}$$

where U_{el} is elastic component of absorbed energy as shown in **Figure 6.4** and η_{el} is elastic geometric factor is dependent on elastic compliance (a/W) but independent of material properties. Thus η_{el} is always exists for converting elastic absorbed energy into elastic J-integral and can be calculated from elastic compliance as [135]

$$\eta_{el} = \frac{1.5 * (1 - \acute{\alpha})\acute{\beta}^2 . f_4'(\acute{\alpha})}{[0.25\acute{\beta}^3 + 0.78\acute{\beta} + 1.5\acute{\beta}^2 . f_4(\acute{\alpha})]} \tag{6.4}$$

where $\acute{\alpha} = a/W$ and $\acute{\beta} = S/W$, $f_4(\acute{\alpha}) = \left(\frac{2\acute{\alpha}}{1-\acute{\alpha}}\right)^2 [5.58 - 19.57\acute{\alpha} + 36.82\acute{\alpha}^2 - 39.94\acute{\alpha}^3 + 12.77\acute{\alpha}^4]$ and $f_4'(\acute{\alpha}) = \frac{2\acute{\alpha}}{(1-\acute{\alpha})^2}[5.58 - 19.57\acute{\alpha} + 36.82\acute{\alpha}^2 - 39.94\acute{\alpha}^3 + 12.77\acute{\alpha}^4] + \left(\frac{\acute{\alpha}}{1-\acute{\alpha}}\right)^2 [-19.57 + 73.64\acute{\alpha} - 104.82\acute{\alpha}^2 + 51.08\acute{\alpha}^3]$.

For the SENB specimen used in the present work, the value of η_{el} is evaluated equal to 1.2044 from the above set of equations. Correspondingly, the experimental J_{Ic} values based on unimodular material model using peak fracture load and the area under the load-displacement curve can be determined.

6.4. Numerical model for Terfenol-D SENB specimen

In order to compute the fracture parameters of the Terfenol-D SENB specimen under an applied external field, a finite element model of the specimen has been created as similar to the experiment based on the ASTM E399. The governing magneto-elastic field equations and solution methodology is remained same as described in Chapter 5. Considering the symmetry of geometry, loading and support condition for the edge cracked SENB fracture specimen quarter-symmetric finite element model is developed for the numerical analysis as displayed in the **Figure 6.5**. Symmetry conditions are imposed on the sectioned boundaries of the specimen (shaded in blue colour in **Figure 6.5**). Note that all the traction components are zero along the crack faces, thus adheres the free boundary condition.

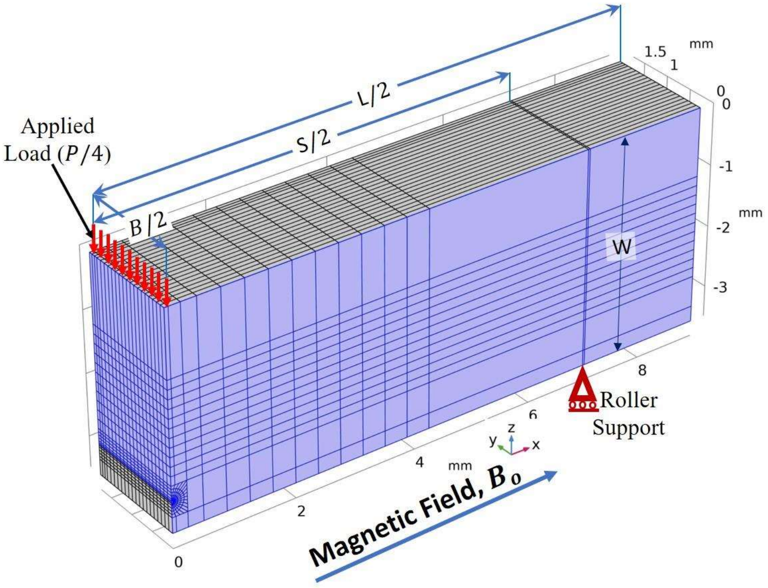

Figure 6.5 Quarter symmetric FE model for single edge specimen in three-point bending (symmetry regions are shaded in blue colour)

A sufficiently large quarter symmetric air domain is built around the specimen to realistically mimic the magnetic flux path as shown in **Figure 6.8**.

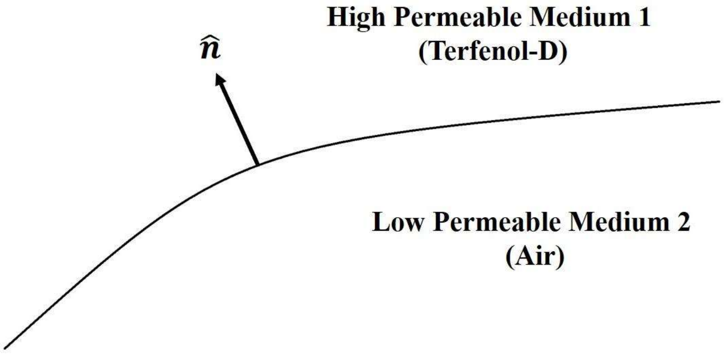

Figure 6.6: *Interface between two mediums.*

The solutions for the differential Maxwell equations given in a domain can be determined by using the appropriate boundary conditions associated with that domain. For a source current free interface between two mediums having relatively high and low permeability respectively as shown in **Figure 6.6**, then the boundary conditions can be written as [70,71]

$$\hat{\boldsymbol{n}} \cdot (\boldsymbol{B_1} - \boldsymbol{B_2}) = 0 \tag{6.5}$$

$$\hat{\boldsymbol{n}} \times (\boldsymbol{H_1} - \boldsymbol{H_2}) = 0 \tag{6.6}$$

Since the external magnetic field is applied in the direction of perpendicular to the crack surface, thus the boundary condition mentioned in Eq. (6.10) applies at crack surface. In the present analysis, the modelling domain possess magnetic symmetry, then we can reduce the model size to minimize the computational efforts and time. We can exploit the geometric symmetry and interfacial magnetic boundary conditions to truncate the modelling domain. Two types of interfacial boundary conditions exist as the magnetic insulation boundary condition and the perfect magnetic conductor boundary condition.

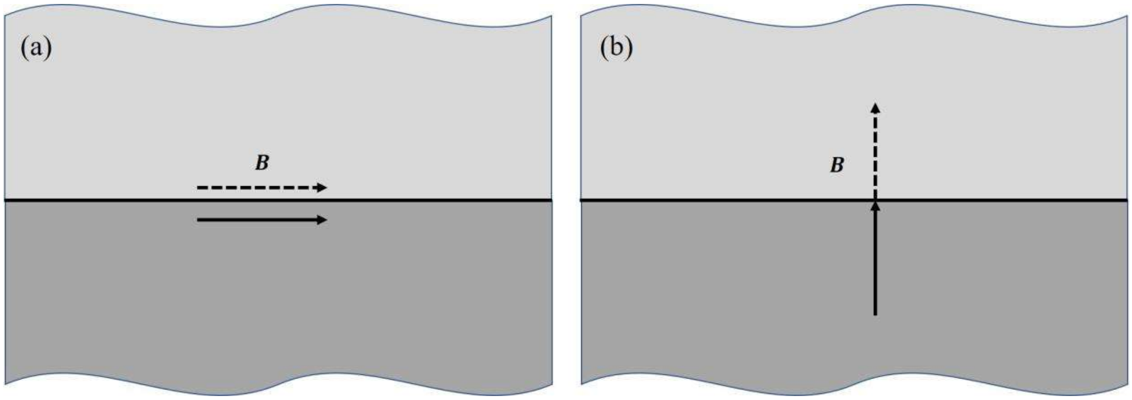

Figure 6.7: ***(a)*** *The magnetic insulation boundary condition* ***(b)*** *The perfect magnetic conductor boundary condition*

The magnetic flux density is tangential to the boundary on the symmetry plane in **Figure 6.8 (a)** and is specified by the magnetic insulation condition (i.e., $\boldsymbol{n} \cdot \boldsymbol{B} = 0$) as shown in **Figure 6.7 (a)**. The magnetic insulation boundary condition shows the exactly mirror symmetry plane for magnetic flux density.

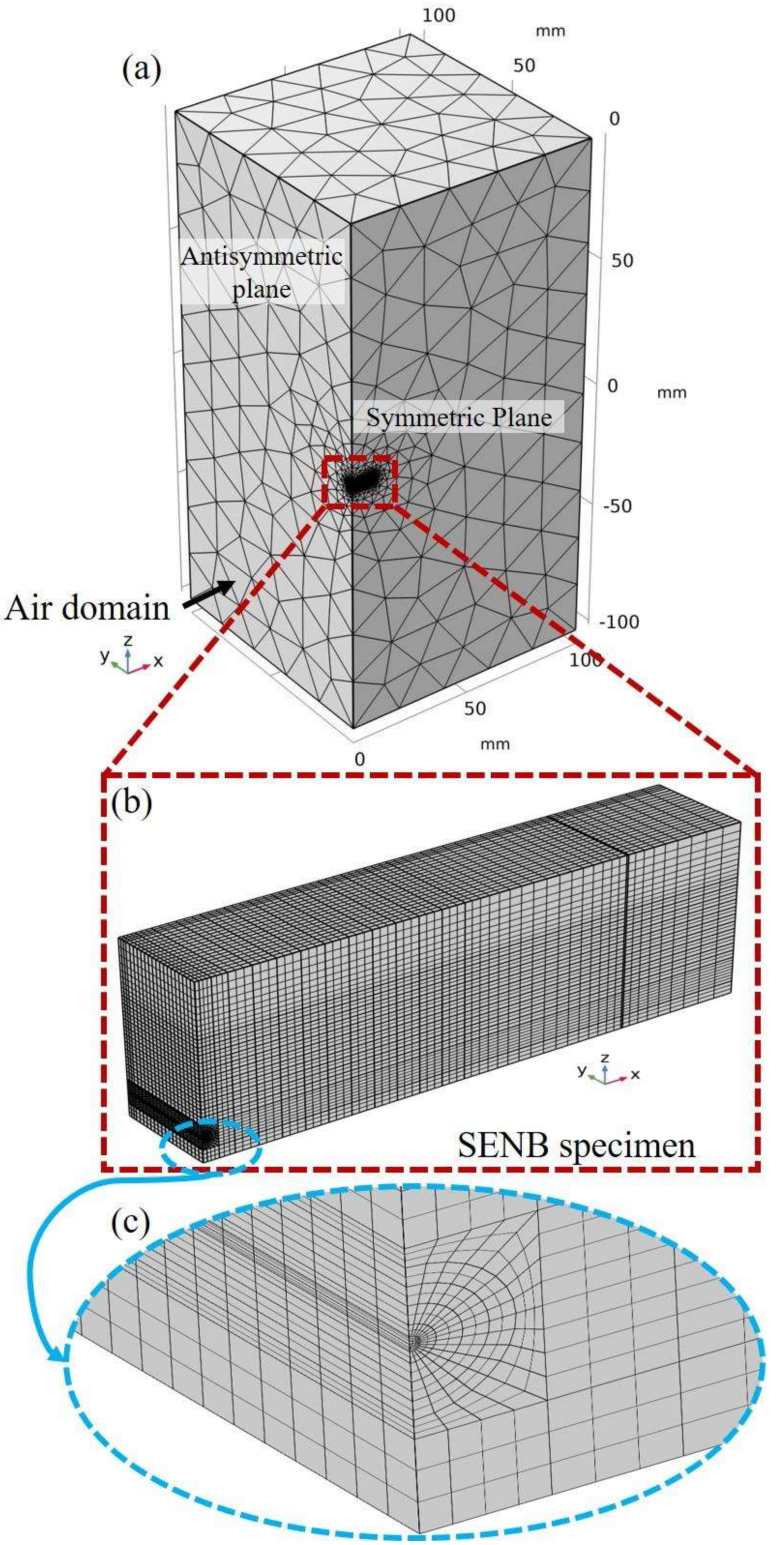

Figure 6.8 FE mesh distribution for the quarter symmetric numerical model of the single edge three-point bend specimen under the externally applied magnetic field **(a)** air domain comprising the specimen **(b)** quarter symmetric specimen **(c)** enlarge view of mesh near the crack tip

On antisymmetric plane, the perfect magnetic conductor boundary condition as shown in **Figure 6.7 (b)** presents a condition that strictly requires the tangential component of the magnetic field to be zero so that the magnetic field only points normal to the interface boundary and does not change sign as we pass it. This condition can be written in form of magnetic field as $\hat{\boldsymbol{n}} \times \boldsymbol{H} = \boldsymbol{0}$**.** In case of zero current density, this boundary condition can be described in the form of magnetic scalar potential as $\varphi_m = 0$ [24,72–75] ahead of the crack faces on the antisymmetric planes. Infinite element domains are employed to minimize the influence on the field in the vicinity of the specimen due to the boundary condition imposed on its remaining exterior boundaries. **Figure 6.8 (a)** illustrates the FE meshing of the quarter-symmetric numerical specimen as well as the circumambient air domain. A pertinent mesh convergence analysis is conducted to optimize the accuracy of the FE model predictions and the computational effort and time.

The meshing of the numerical specimen illustrated in **Figure 6.8 (b)** typically comprises 59430 hexahedron elements generated using the swept mesh. Scientifically prudent mesh grading and refinement were performed near the crack tip area to observe the singularity in the stress field, as shown in **Figure 6.8 (c).** The air domain that comes into contact with the numerical specimen is meshed to facilitate 92934 tetrahedron elements with the help of 6358 pyramid elements.

6.4.1. Finite element computation procedure for J-integral

The intricate final form of the derived J-integral necessitates efficient computational tools to estimate the critical energy release rate (J_{Ic}). Since the Terfenol-D is quite brittle and has no plasticity effects in the crack propagation process, a nonlinear elastic analysis seems sufficient. In the presence of manufacturing flaws or cracks, Terfenol-D has a substantially lower tensile strength than its compressive strength, making it susceptible to in-service failures. The rigors of nonlinear stress field formulation near the fracture process zone to quantify the 3-D crack propagation behaviour may exclude its adoption in the elementary design of smart devices. However, a cataclysm may be better planned with a certain degree of reliability preceding computing effort in consideration of the unprecedented ambiguity in high-risk intelligent device applications.

An estimation method for the 3-D path independent integral in a brittle giant magnetostrictive material is described in this sub-section. For the convenience of further discussions, the $J_1^n(s)$ (from Eq. (4.23)) can be separated into its constituent integrals as

$$J_1(C) = \int_{\Gamma} \mathcal{W}^e n_1 d\Gamma \tag{6.7}$$

$$J_2(C) = -\int_{\Gamma} \sigma_{ij} n_j u_{i,1} d\Gamma \tag{6.8}$$

$$J_1(A) = -\int_{A_1} \frac{\partial}{\partial X_3}\left(\sigma_{i3} u_{i,1}\right) dA \tag{6.9}$$

$$J_2(A) = \int_{A_1} \sigma_{ij} \left(\frac{\partial \varepsilon_{ij}^{n}}{\partial X_1}\right) dA \tag{6.10}$$

$$J_3(A) = \int_{A_1} \sigma_{ij} \left(\frac{\partial \varepsilon_{ij}^{m}}{\partial X_1}\right) dA \tag{6.11}$$

$$J_4(A) = \int_{A_1} \rho \ddot{u}_i u_{i,1} dA \tag{6.12}$$

$$J_5(A) = -\int_{A_1} M_j \frac{\partial B_{0i}}{\partial X_j} u_{i,1} dA \tag{6.13}$$

The quarter symmetric numerical specimen with a single edge notch of length ‘*a*’ is subjected to three-point bending as described in previous section. The parallelepiped elements are implemented across the crack front to eliminate the error caused by the crack to width ratio dependency and thickness effect in comparison to 2-D analysis. The ensuing deformation in the specimen is functionally reliant on the stress characteristics and the distribution of magnetization. The contour and area integrals are evaluated over the 21 sections which are parallel to the xz plane of the quarter symmetric numerical specimen as shown in **Figure 6.9.** In this investigation, the 3-D fracture parameter J is computed for thirteen different contours and areas, spanning thirteen different locations surrounding the crack tip in their respective planes. As a result, a total of 130 integration routes are employed to meticulously characterize the fracture strength across the entire domain. In the ongoing numerical simulation, the x, y and z-directions correspond to the X_1, X_3 and X_2 co-ordinates, respectively. Here specifically to keep consistency with the derived mathematical formulations, y-direction has been considered as X_3.

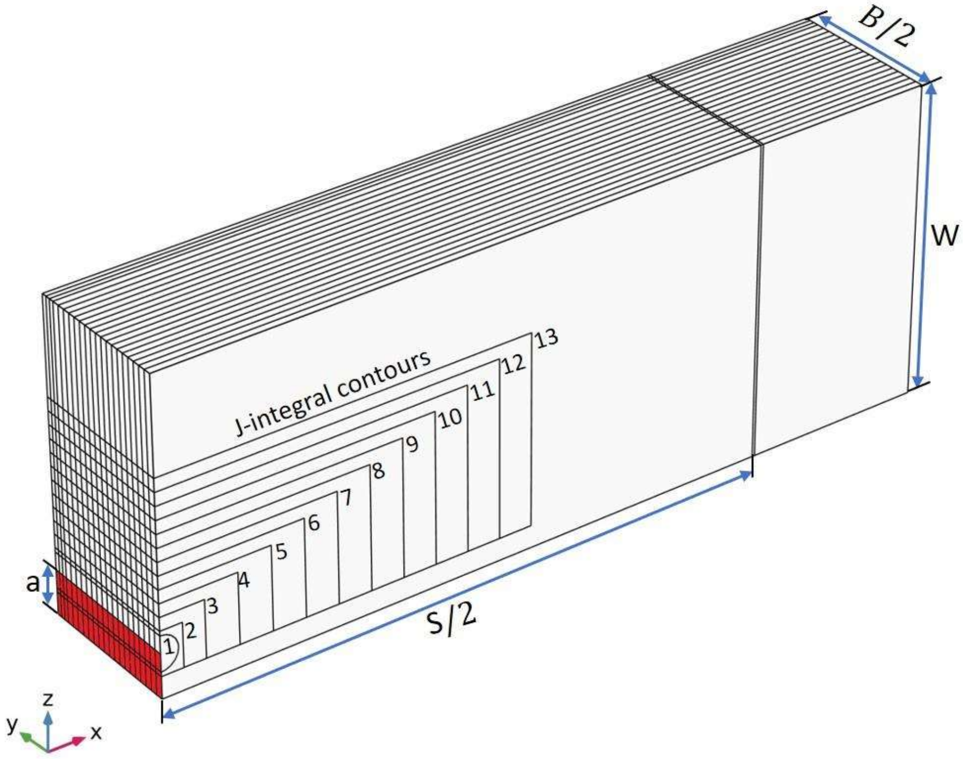

Figure 6.9 Contours for J-integral evaluation

Beginning with the symmetrical mid-plane surface, the contour integral is evaluated at the intersection of the common surface of adjacent elements with the vertical xz plane. On each plane, the line integration operators are defined for each contour and the global expressions of $J_1(C)$ and $J_2(C)$ are setting up for the calculation of path integration. It is worth noting that the boundaries of the crack front are not included in the J-integral evaluation since all the traction components are zero as the crack faces are not loaded. When computing the J-integral, the normal of contour must point outward of the region which the contour encompasses. To ensure that this is the case, a local normal variable whose sign can be inverted when necessary is defined. The area integration operators are setting up on the area delineated by each contour that encloses the crack front, is utilized to evaluate the area integrals on every plane. The global expressions of the $J_2(A)$, $J_3(A)$, $J_4(A)$ and $J_5(A)$ area integrals are established for computation. To compute $J_1(A)$, the quantity $\sigma_{i3}u_{i,1}$ is formed on the element nodes of each area. The linear interpolation function has been employed to define the variation of the nodal values over the element. The derivatives with respect to X_3 (or y-direction with reference to **Figure 6.9**) are then evaluated using the standard techniques.

The accuracy of this coupled physics 3-D problem for evaluating the nonlinearity in strain distribution iteratively is hugely mesh sensitive and depends on number of iterations. The bi-nonlinear phenomenon can indeed be noticed in the 3-point bend simulation of the SENB specimen because of the nonuniform tension and compression regions.

6.5. Results and discussions

In this section, the effect of magnetization and the nonlinear stress-strain relationship on the measurement of the critical strain energy J_{Ic} is examined. This study process involves the three-point bend test on SENB fracture specimens and correspondingly the appropriate numerical simulations in the three-dimensional realm. Table 6-1 presents the experimental results of the peak fracture load (P_{max}) of one set (two specimens) of Terfenol-D SENB specimens in the presence and absence of the magnetic field. The peak fracture load values for each set of SENB specimens prepared from a single Terfenol-D cuboid are tabulated in adjacent columns. As noted in **Table 6-1** the significant decrement in the fracture loads is observed in the presence of magnetic field (0.03 T) for each set. Peak fracture load datasets acquired from the 3-point flexural tests are then incorporated into two parameter Weibull statistical model and the mean value for the failure (Weibull characteristic strength) has been predicted. The mean peak fracture load and the load-displacement curve for the cracked specimens of magnetostrictive Terfenol-D are then used to evaluate the experimental J_{Ic} values based on unimodular material model and the area under the load-displacement curve (i.e., fracture energy absorbed by specimen) and tabulated in **Table 6-1**. Then magneto-elasticity coupled 3-D finite element analyses are performed to compute the corresponding path independent J-integrals numerically.

The determined values of the experimental J_{Ic} of the Terfenol-D reflects an analogous decrement rather than being a constant fracture toughness quantity based on unimodular material assumption, which is contradicting, as Terfenol-D shows the stress and magnetization dependent variable elasticity characteristics (ΔE effect). The nonlinear elastic characteristic in Terfenol-D along with the varied coupled magneto-elastic loading has been hypothesized to be a plausible contributor to the reduction in fracture load. The significance of the nonlinear stress-strain relationship has been substantiated by numerical investigations based on linear and nonlinear elasticity theory. The next sub-sections discuss the relevant findings implicating the apprehensions.

Table 6-1 Peak fracture load datasets obtained from (SE) three-point flexure experiments

Specimen No.	$B_o = 0\,T$			$B_o = 0.03\,T$		
	Peak Fracture Load, P_{max} (N)	J_{Ic} (Based on the unimodular material model), (N/m)	J_{Ic} (Based on the elastic component of absorbed energy), (N/m)	Peak Fracture Load, P_{max} (N)	J_{Ic} (Based on the unimodular material model), (N/m)	J_{Ic} (Based on the elastic component of absorbed energy), (N/m)
1	44.63	7.65	12.66	40.56	6.32	15.02
2	48.72	9.12	13.85	37.82	5.50	14.03
3	50.85	9.94	14.45	46.06	8.15	17.08
4	53.24	10.89	15.19	44.17	7.50	16.45
5	55.46	11.82	15.89	49.18	9.29	18.38
6	57.46	12.68	16.31	47.38	8.63	17.55
7	59.55	13.62	16.93	45.44	7.93	16.85
8	52.37	10.54	14.85	50.82	9.92	18.80
9	46.76	8.40	13.25	39.30	5.94	14.53
10	58.36	13.08	16.50	47.90	8.82	17.67
11	42.11	6.81	12.04	34.33	4.53	12.80
12	53.92	11.17	15.40	46.44	8.29	17.31
13	55.79	11.96	15.94	48.55	9.06	18.13
14	57.9	12.88	16.54	50.52	9.81	18.79
15	47.38	8.63	13.54	42.92	7.08	15.92
16	40.29	6.24	11.51	38.09	5.58	14.11
17	56.61	12.31	16.17	48.69	9.11	18.02
18	43.36	7.23	12.39	36.65	5.16	13.59
19	60.61	14.11	17.32	51.35	10.13	19.04
20	48.33	8.98	13.81	41.68	6.68	15.52
21	51.69	10.27	14.77	45.21	7.85	16.92
22	56.7	12.35	16.20	49.07	9.25	18.17
23	45.44	7.93	12.98	35.4	4.82	13.13
24	50.2	9.68	14.34	43.8	7.37	16.20
25	52.46	10.57	14.99	45.81	8.06	16.93
26	55.75	11.94	15.93	46.84	8.43	17.28
27	53.75	11.1	15.36	46.25	8.22	17.25
28	51.42	10.16	14.69	43.02	7.11	16.04
29	49.03	9.24	14.01	44.72	7.69	16.70
30	54.4	11.37	15.54	49.97	9.59	18.59

6.5.1. Weibull statistical theory in the estimation of peak fracture load

The nonlinear modulus of giant magnetostrictive materials (e.g., Terfenol-D) in their operating regimes is different in tension and compression. Considering the effect of nonlinear modularity, the fracture strength of single edge notched specimens is characterized by the peak fracture load (P_{max}). The fracture parameter critical strain energy release rate (J_{Ic}) is computed using the peak load values and nonlinear constitutive relations in the finite element simulation. The experimental critical strain energy release rate values, calculated assuming the specimen as unimodular, are compared with the numerical simulation results to investigate the influence of nonlinear modularity.

Experimental evaluation of peak fracture load (P_{max} shown in **Table 6-1**) of Terfenol-D SENB specimens in the presence and absence of the magnetic field confirms the unpredictable variability of the fracture strength even if identical loading conditions are maintained for both. For a sustainable design of intelligent devices, the peak load (P_{max}) must be quantified in their functional magnetic field regimes. This requires an appropriate probabilistic technique to characterize the fracture strength of Terfenol-D that fails in a brittle manner. Consequently, the Weibull statistical strength theory based on weakest link philosophy was employed to predict the probability of failure (or, alternately, the fracture strength) of the Terfenol-D in magneto-elastic stimuli environment. In the Weibull strength analysis, the three-parameter cumulative probability function for the probability of failure P_f is written as [102,103]:

$$P_f = 1 - exp\left[-\left(\frac{P_{max} - P_u}{P_\theta}\right)^m\right] \qquad P_{max} > 0 \tag{6.14}$$

$$P_f = 0 \qquad P_{max} \leq 0 \tag{6.15}$$

where, P_u is the threshold load parameter representing the lowest load value below which test specimen will not fracture. The scale parameter P_θ is the characteristic strength with dependence on the loading configuration. Weibull modulus m is the distribution shape parameter. The three-parameter Weibull model is used to define extreme functions. For strength characterization two parameter Weibull model is sufficient in stochastic fracture theory. In the three-parameter Weibull model P_u might denote the dataset's lower bound. This is suitable for a dataset that has been extensively examined to remove flaws over a specific lot or coupon size. Thus, assuming a limiting threshold strength exists without proper screening or non-destructive assessment is exceedingly parlous. The two-parameter Weibull distribution is yielded by setting $P_u = 0$ in Eqn. (6.14) as per ASTM C1239-13 [128]

$$P_f = 1 - exp\left[-\left(\frac{P_{max}}{P_\theta}\right)^m\right] \qquad P_{max} > 0 \qquad (6.16)$$

$$P_f = 0 \qquad P_{max} \leq 0 \qquad (6.17)$$

We can deduce the probability density function $f(P_{max})$ as the first derivative of Eqs. (6.16) and (6.17) in the form of following expressions:

$$f(P_{max}) = \left(\frac{m}{P_\theta}\right)\left(\frac{P_{max}}{P_\theta}\right)^{m-1} exp\left[-\left(\frac{P_{max}}{P_\theta}\right)^m\right] \qquad P_{max} > 0 \qquad (6.18)$$

$$f(P_{max}) = 0 \qquad P_{max} \leq 0 \qquad (6.19)$$

and taking the double logarithm of resultant two-parameter Weibull distribution following the rearrangement of Eqn. (6.18) gives

$$ln(1 - P_f) = -\left(\frac{P_{max}}{P_\theta}\right)^m \qquad P_{max} > 0 \qquad (6.20)$$

$$ln\left[ln\left(\frac{1}{(1-P_f)}\right)\right] = m\, ln\, P_{max} - m\, ln\, P_\theta \qquad P_{max} > 0 \qquad (6.21)$$

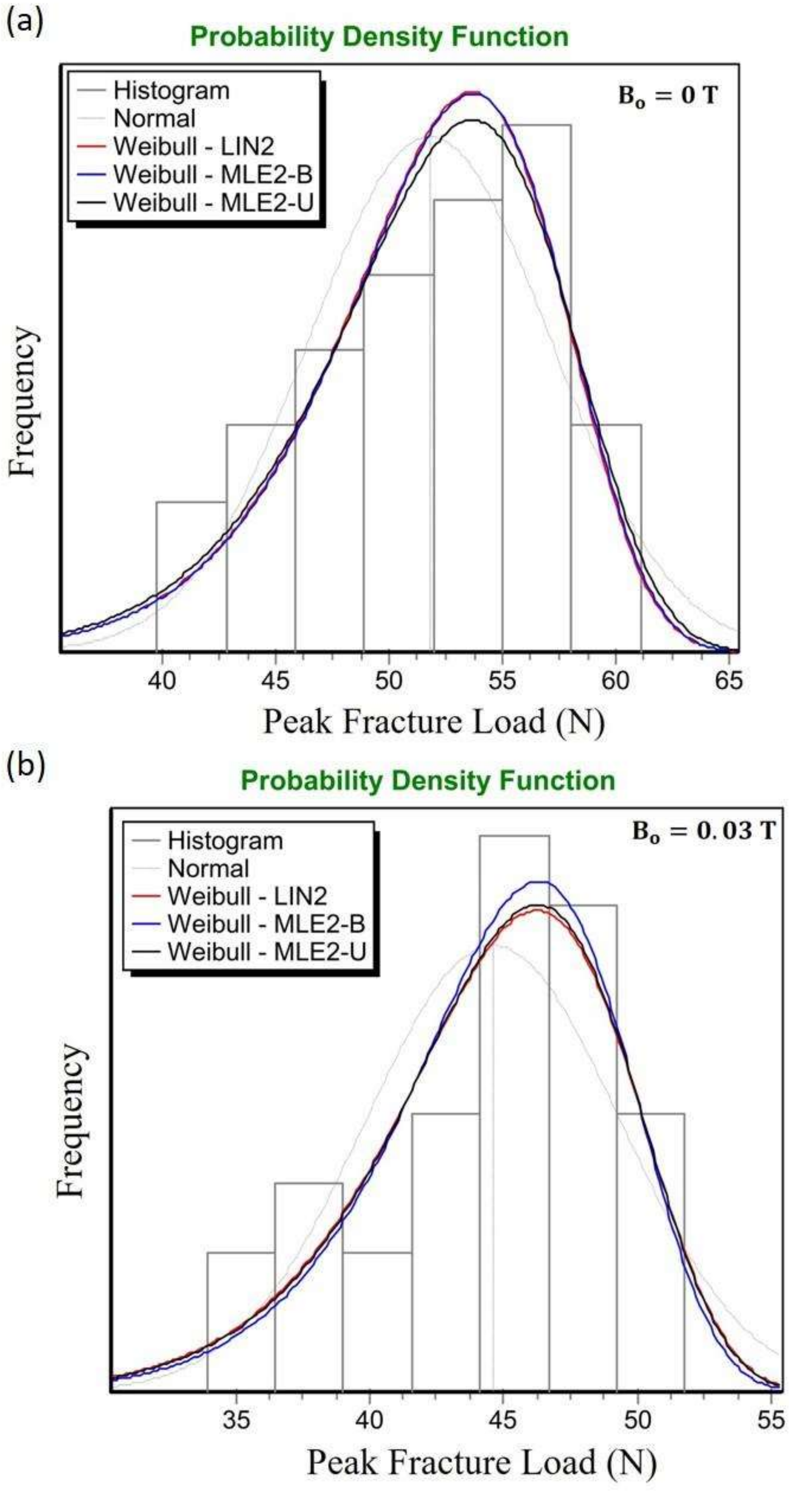

Figure 6.10: The probability density function plot with random peak fracture load dataset obtained for the Terfenol-D SENB specimens **(a)** in absence of magnetic field and **(b)** in presence of 0.03 T magnetic field using Weibull and Normal distribution.

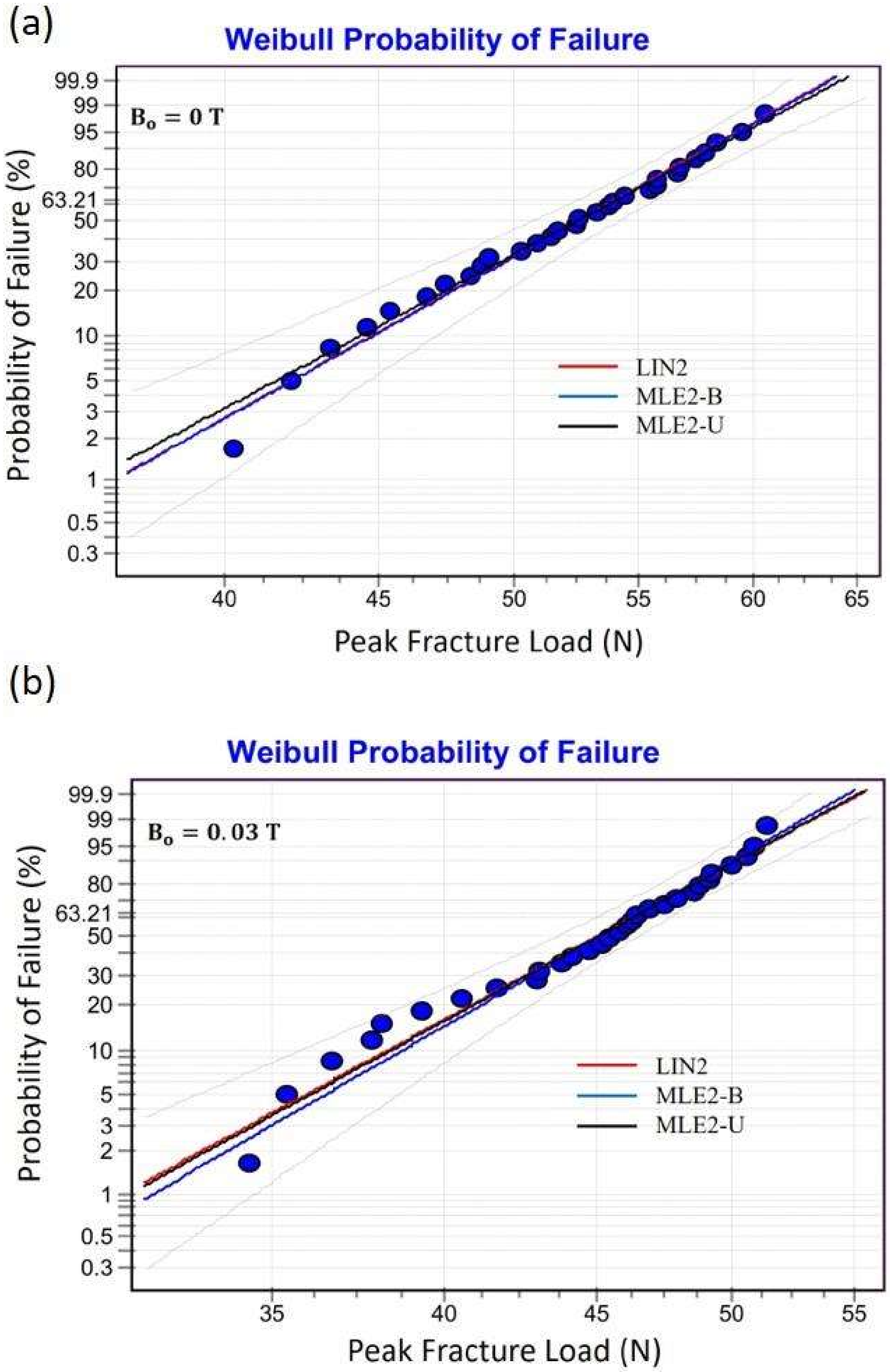

Figure 6.11: Weibull distribution plot for peak fracture load dataset obtained for the Terfenol-D SENB specimens and the best fit line drawn with LIN2, MLE2-B and MLE2-U estimators **(a)** in absence of magnetic field **(b)** in presence of 0.03 T magnetic field.

When the left side of Eqn. (6.21) is equal to zero, the characteristic strength (P_θ) is the strength value, P_{max} at $P_f = 63.21\%$. **Figure 6.10** shows the variation of the probability density function $f(P_{max})$ against the Peak fracture load obtained from the experimental data. A simple linear regression analysis is generally adequate to evaluate the Weibull parameters but the superior maximum likelihood estimation (MLE) approach outperforms the linear regression methods in the determination of the parameters (*m,* P_θ) from a set of fracture loads [29]. To predict the failure probability of each data, linear regression using the least square estimator necessitates the application of a ranking criteria for every fracture load data. The failure data are regressed to get the distribution parameters, once an estimate of individual probability is determined. The peak fracture load data from the experiments were initially ranked in ascending order and ranked cumulative probability of failure (P_f) is allocated to each data according to a low bias estimator as follows [29,128]:

$$P_f\left(P_{max_i}\right) = \frac{i - 0.5}{n} \tag{6.22}$$

where i is the rank of the i^{th} data point and n is the total number of SENB specimens.

To estimate the exclusive critical strain energy release rate (J_{Ic}), cumulative probability distribution plot of failure load data was plotted against the peak fracture load as shown in **Figure 6.11**. The natural logarithm of the i^{th} peak fracture load data and the double natural logarithm of $\left[1/\left(1 - P_f\right)\right]$ is computed for this purpose. In the graph $\ln\left[\ln\left(1/\left(1 - P_f\right)\right)\right]$ is plotted as the ordinate and $\ln(P_{max})$ as the abscissa. The maximum likelihood technique has several advantages, one of which is that its parameter estimation for the two-parameter Weibull distribution is unique. The estimation statistically approximates the true values of the population as the sample size grows. Let P_{max_1}, P_{max_2}, ……………P_{max_n} reflect the peak fracture load (a random variable) of the Terfenol-D SENB specimens in a given sample data set and the two-parameter Weibull distribution is assumed to characterize the peak fracture load. The joint density of the n random variables is the likelihood function associated with this sample dataset and hence is a function of the two unknown distribution parameters (m, P_θ). The likelihood function for the two parameter Weibull distribution for uncensored population is then given by the following expression [128]

$$L = \prod_{i=1}^{n} \left(\frac{m}{P_\theta}\right)\left(\frac{P_{max_i}}{P_\theta}\right)^{m-1} exp\left[-\left(\frac{P_{max_i}}{P_\theta}\right)^{m}\right] \tag{6.23}$$

The Weibull modulus (m) and scale parameter (P_θ) can be determined by evaluating the partial derivatives of the logarithm of the likelihood function with respect to Weibull parameters (m, P_θ) and equating the resulting expressions to zero. For an uncensored population, the equations derived by differentiating the log likelihood function is given as

$$\frac{\sum_{i=1}^{n}\left(P_{max_i}\right)^m ln\, P_{max_i}}{\sum_{i=1}^{n}\left(P_{max_i}\right)^m} - \frac{1}{n}\sum_{i=1}^{n} ln\, P_{max_i} - \frac{1}{m} = 0 \tag{6.24}$$

$$P_\theta = \left[\left(\sum_{i=1}^{n}\left(P_{max_i}\right)^m\right)\frac{1}{n}\right]^{\frac{1}{m}} \tag{6.25}$$

Initially the WeibPar 4.3 program (Procured from Connecticut Reserve Technology) solves Eq. (6.24) for Weibull modulus (m) using numerical iteration and then using the value of m in Eq. (6.25) P_θ is evaluated directly. Since critical strain energy release rate (J_{Ic}) is a material property defining the resistance to progressive crack propagation; hence it becomes mandatory to forecast a unique J_{Ic} value for the material in the magneto-elastic environment. This can be achieved by plotting the probability of failure against both (with and without magnetic field) the normalized peak fracture load data set with 90% confidence bound based on the Weibull model as shown in **Figure 6.11**. The best fit line generated by biased (MLE2-B), unbiased (MLE2-U) maximum likelihood estimators, and the least square (LIN2) estimator procedure are used to examine the variable dataset on the Weibull graph. The efficacy of fitting the normalized sample population in the Weibull distribution helps us to enhance the base for the estimates of the variability. It is reasonable to infer that both the normalized dataset obtained from the fracture test in presence and absence of the magnetic field, follows the Weibull probability distribution as all the scatter peak load data points are close to the reference line. **Figure 6.10** display the histogram plots of Weibull and Normal probability density function with the peak fracture load for both datasets. This plot suggests that all the three estimators along with the Weibull distribution can fit the peak load fracture datasets adequately in comparison to the Normal distribution.

Table 6-2: Co-efficient of determination (R^2), Weibull modulus and mean characteristic load parameter with Weibull distribution in different externally applied magnetic field.

External Magnetic field	Estimator	R^2 value	Weibull modulus (m)	mean peak fracture load (P_θ)
0 T	LIN2	0.98536	11.8905	54.063
	MLE2B	0.98524	11.8689	54.129
	MLE2U	*0.98267*	*11.3114*	*54.134*
0.03 T	LIN2	0.97341	11.4112	46.601
	MLE2B	0.96935	12.1113	46.612
	MLE2U	*0.97321*	*11.5425*	*46.616*

Table 6-2 lists the Weibull parameters and goodness of fit (R^2) for Weibull probability distributions for both datasets calculated using all the three estimators. The mean value of peak fracture load dataset evaluated from all three distribution estimators falls within a narrow range for each case. The mean value of peak fracture loads (i.e., 54.134 N and 46.616 N in the absence and presence of the magnetic field respectively) determined from the unbiased (MLE2-U) maximum likelihood estimator has been further used in the subsequent section for the computation of the critical strain energy release rate (J_{Ic}) of the Terfenol-D specimen.

6.5.2. Experimental results for J_{Ic}

Table 6-3: Mean experimental critical energy release rate (J_{Ic}) values

$\mathbf{B_o = 0\ T}$		$\mathbf{B_o = 0.03\ T}$	
J_{Ic} (Based on the unimodular material model), (N/m)	J_{Ic} (Based on the elastic component of absorbed energy), (N/m)	J_{Ic} (Based on the unimodular material model), (N/m)	J_{Ic} (Based on the elastic component of absorbed energy), (N/m)
11.254	15.45	7.454	17.31

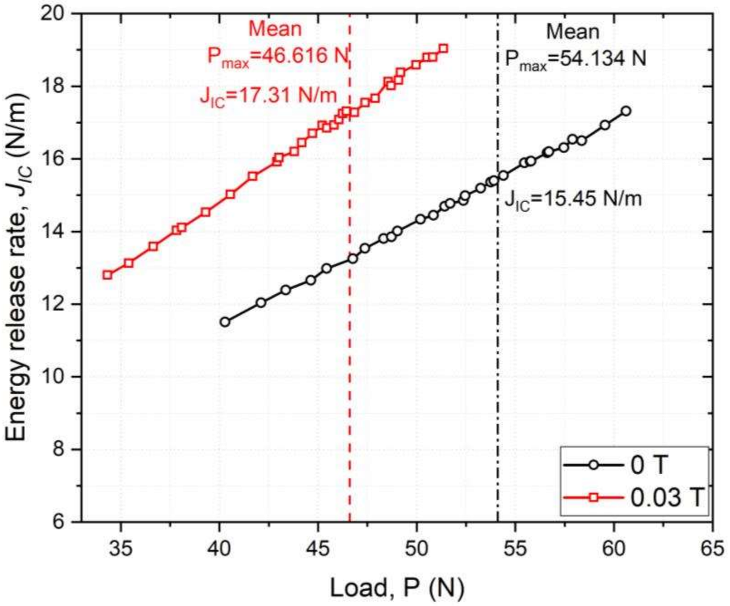

Figure 6.12: Experimental energy release rate (J_{Ic}) values based on the elastic component of absorbed energy with respect to peak fracture load

The experimental energy release rate J_{Ic} is evaluated by using the statistically determined mean peak fracture loads of 54.134 N and 46.616 N in the absence and presence of a magnetic field, respectively. Table 6-3 displays the mean of the experimental critical energy release rate (J_{Ic}) values derived from Eqs. (6.1) and (6.2), assuming the specimen follows the linear stress-strain relationship. The experimental J_{Ic} values based on the area under the load-displacement curve are plotted against the peak fracture load obtained in load-displacement plot in **Figure 6.12**. Then corresponding to the statistically determined mean peak fracture loads in the absence and presence of a magnetic field, two vertical straight lines are drawn such that it intersects the respective curves. Then the respective intersection points give the specific fracture parameter J_{Ic} for the bi-nonlinear Terfenol-D specimen and tabulated in **Table 6-3**.

6.5.3. Numerical results for J_{Ic}

Based on the verified finite element study on the coupled field hysteretic nonlinear constitutive model as implemented in Chapter 5, a numerical three-point bend simulations were established for smooth edge cracked specimens. **Table 5-1** lists the experimental and physics-based optimal materials properties that were used. The mean peak fracture loads were estimated using Weibull two parameter probability model with unbiased maximum likelihood estimator. The statistically estimated mean peak fracture loads of 54.134 N and 46.616 N were employed as mechanical loading conditions in the absence and presence of a magnetic field, respectively. The numerical specimen for the SENB three-point bend fracture tests was built to closely resemble the experimental specimen as per ASTM E1820. **Figure 6.2 (a)** depicts the geometry of the specimen. Section 6.4 demonstrates the finite element meshing for the numerical specimen that are used for the comparison of the linear and nonlinear stress-strain field effect on the critical strain energy release rate (J_{Ic}). Since the stress field's nonlinearity is prevalent in the z-direction, 42 divisions are made in this direction whereas in the y-direction 21 divisions are taken to deduce the variation of J_{Ic} through the thickness.

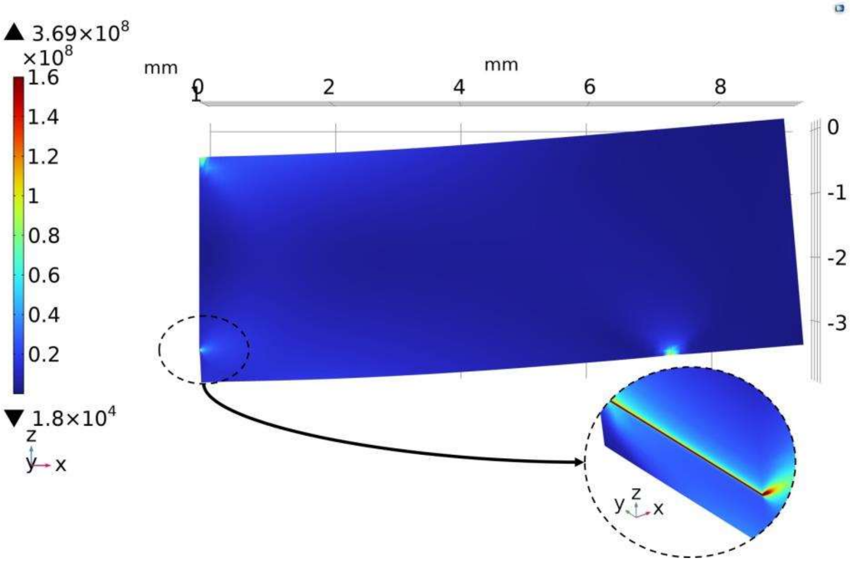

Figure 6.13: Von-Mises stress (in Pa) distribution in the quarter symmetric Terfenol-D specimen at 0.03T and subjected to mean peak load 46.616N

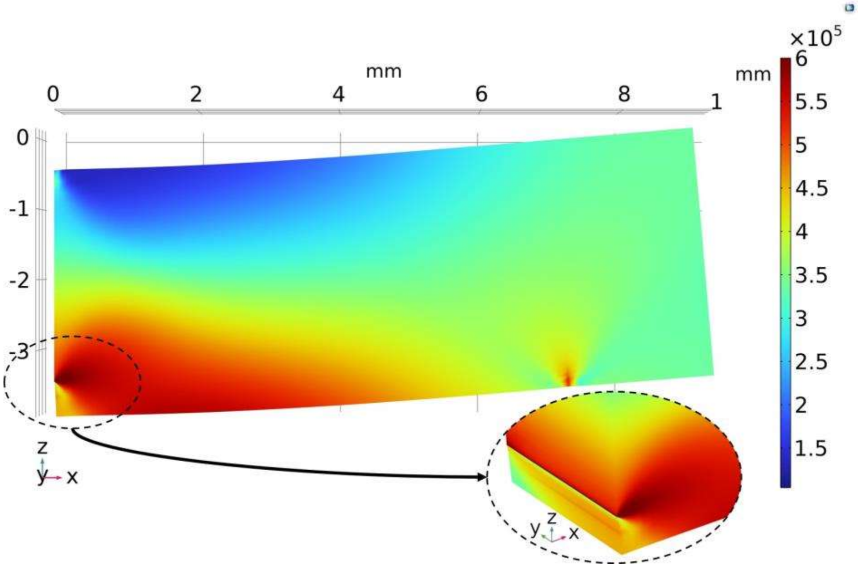

Figure 6.14: Magnetization (in A/m) distribution in the quarter symmetric Terfenol-D specimen at 0.03 T and subjected to mean peak load 46.616 N.

Figure 6.13 and **Figure 6.14** show the Von-Mises stress distribution and the magnetization pattern in the numerical specimen of Terfenol-D with an applied field of 0.03T and a mean peak load of 46.616 N, respectively. It is readily evident from the Von-Mises stress illustration that the singular stresses are present in the vicinity of the crack front. The simulated graph of magnetization distribution demonstrates that the specimen's magnetization adheres to distinct values depending on whether it is in the tensile or compressive zone. This phenomenon is attributed to the change in magnetic anisotropy produced by flexure stresses in positive magnetostrictive materials. The changes in magnetic anisotropy can be explained based on the magnetic domain rotations. Precisely, the flexure tensile stresses tend to align the spin distributions parallel to the longitudinally applied magnetic field; consequently, magnetization saturation occurs faster. In contrast, the flexure compressive stresses tend to orient them in a plane at right angles to the longitudinal direction; thus, the magnetization process becomes more arduous. As illustrated in **Figure 6.14**, the magnetization values approaching saturation near the crack front region reaffirm the consistency of the domain analysis.

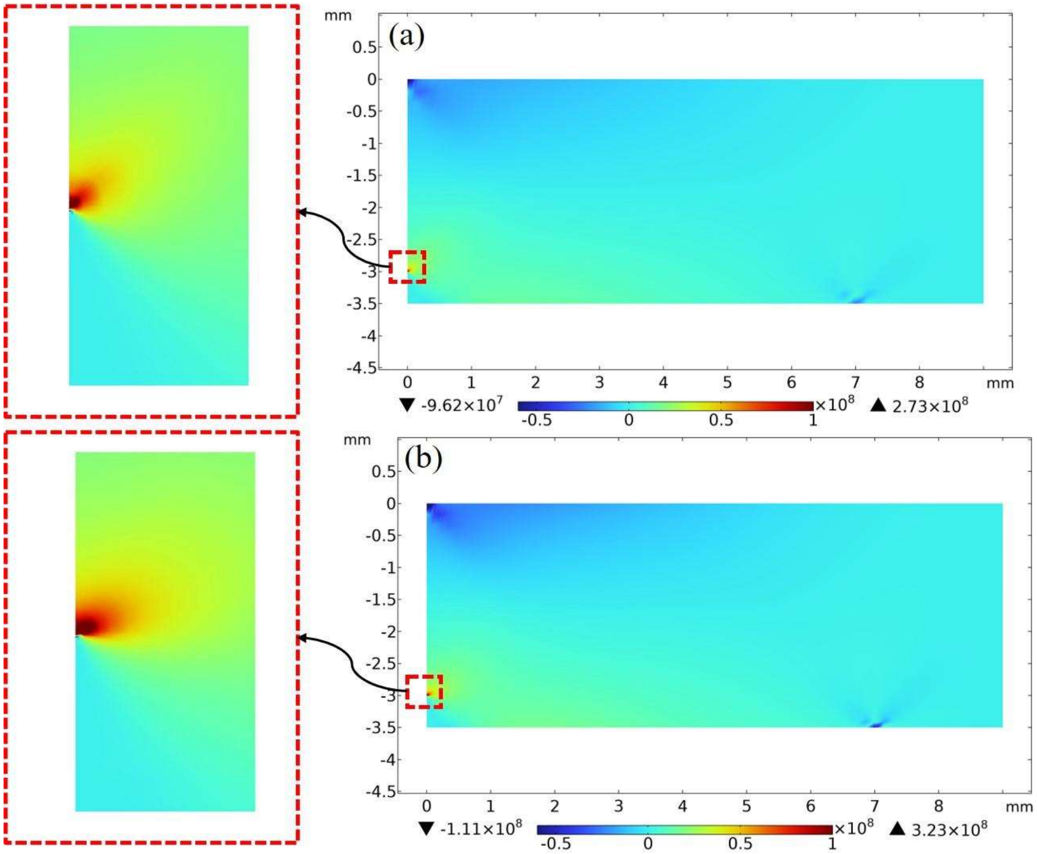

Figure 6.15: Comparison of stress (in Pa) component in x-direction distribution at the mid-plane of numerical specimen when subjected to load 46.616N **(a)** in absence of magnetic field **(b)** in presence of 0.03 T magnetic field.

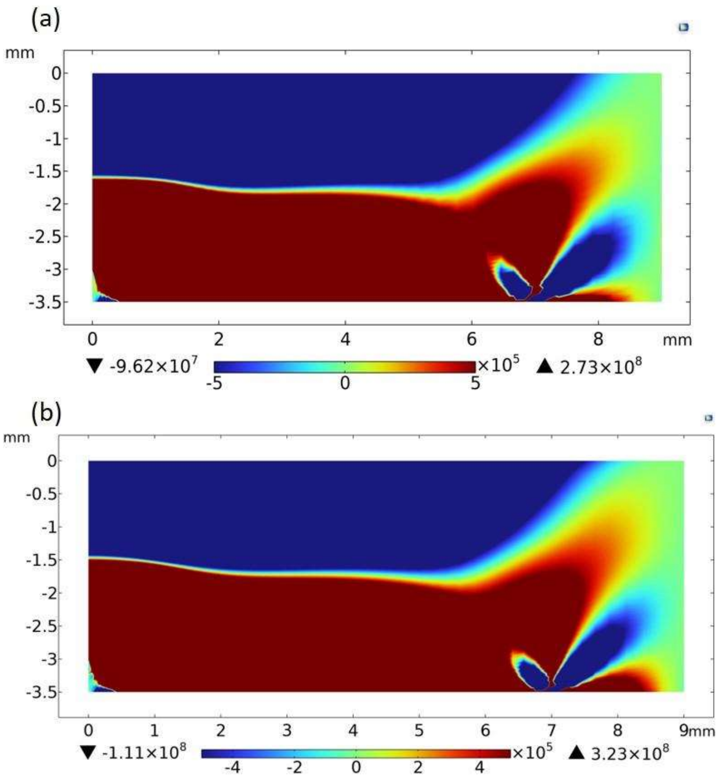

Figure 6.16: Stress (in Pa) component in x-direction distribution at the mid-plane of numerical specimen **(a)** in absence of magnetic field and subjected to fracture load 54.134N **(b)** in presence of 0.03 T magnetic field and subjected to fracture load 46.616N

Figure 6.15 shows the effect of the magnetic field on the stress field distribution in the numerical specimen of Terfenol-D with and without an applied field of 0.03T. The stress field distribution is plotted at the same load level (i.e., 46.616 N) in both the absence and presence of a magnetic field for comparison purposes. An increment in the stress field is seen when a magnetic field of 0.03 T is applied. This change can be visualized more clearly near the crack tip in the zoomed-view plots of each case. **Figure 6.16** depicts the tensile and compressive zones in the midplane of the numerical specimen. The stress contour graphics clearly show a shifting of the neutral axis due to inherent nonlinearity induced by domain rotation and magneto-elastic interactions. The 3D J-integral was computed by utilizing the input parameters, and the values of its constitutive integrals were determined for all thirteen contours in each cross-sectional xz-plane. The contour integrals $J_1(C)$, $J_2(C)$ and area integrals $J_2(A)$, $J_3(A)$ are evaluated solely at the different cross-sectional xz-planes (i.e., located at $2y/B = 0.1, 0.6, 0.8, 0.91, 0.99$) of the specimen in the absence and presence of the magnetic field. The variation of the contour integral $J_1(C) + J_2(C)$ at the different cross-sectional planes is plotted in **Figure 6.17**, which displays the noticeable incremental variations with the increasing integration contours in x-direction, notably close to the outer surface. The area integral terms $J_2(A)$ and $J_3(A)$ are depends on the nonlinear strain term ε_{ij}^{n} and magnetostrictive strain term ε_{ij}^{m}, respectively. **Figure 6.18 (a)** shows the variation of $J_2(A)$, $J_3(A)$ in presence of applied field, whereas, **Figure 6.18 (b)** shows the variation of $J_2(A)$ only, as the value of $J_3(A)$ is vanished in the absence of applied magnetic field. The values of $J_2(A)$ and $J_3(A)$ demonstrates the substantial decreasing pattern with the increasing integration contours for all the through thickness evaluation planes. The values of the total contour and area integral i.e., $J_1(C) + J_2(C) + J_2(A) + J_3(A)$ evaluated solely at the different cross-sectional xz-planes are plotted with different integration contours in the increasing x-direction as shown in **Figure 6.19**. The $J_1(C) + J_2(C) + J_2(A) + J_3(A)$ values exhibit a distinguishable variance with x-direction, particularly adjacent to the free surfaces. In proximity to the mid-plane (i.e., $2y/B = 0.1$) the $J_1(C) + J_2(C) + J_2(A) + J_3(A)$ values vary gradually with x-direction. It can be noted that the presence of a magnetic field amplifies the variation of integral values in the Terfenol-D specimen owing to magneto-elastic effects.

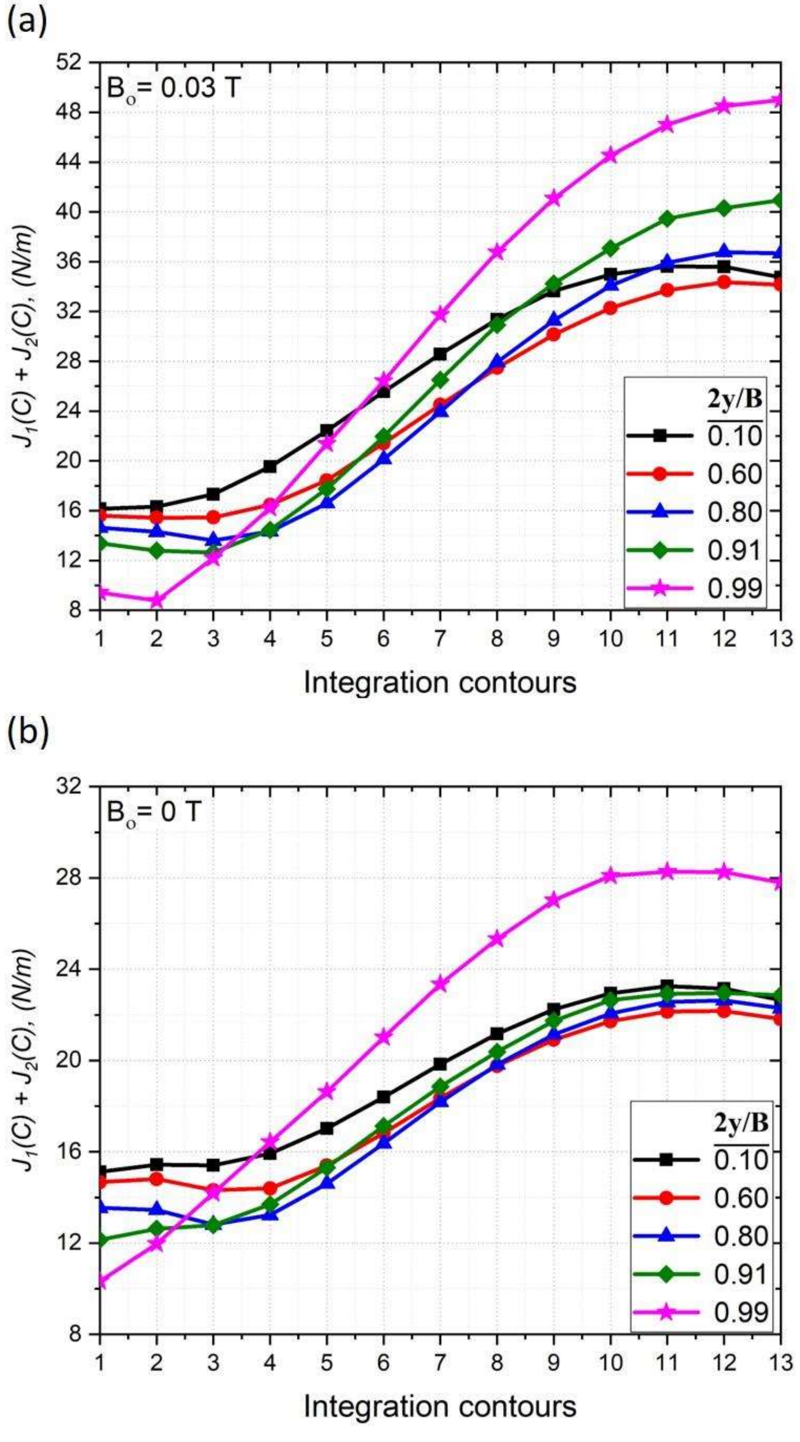

Figure 6.17: Variation of $J_1(C) + J_2(C)$ at different cross-sectional planes under (a) $B_o = 0.03\ T$ and (b) $B_o = 0\ T$

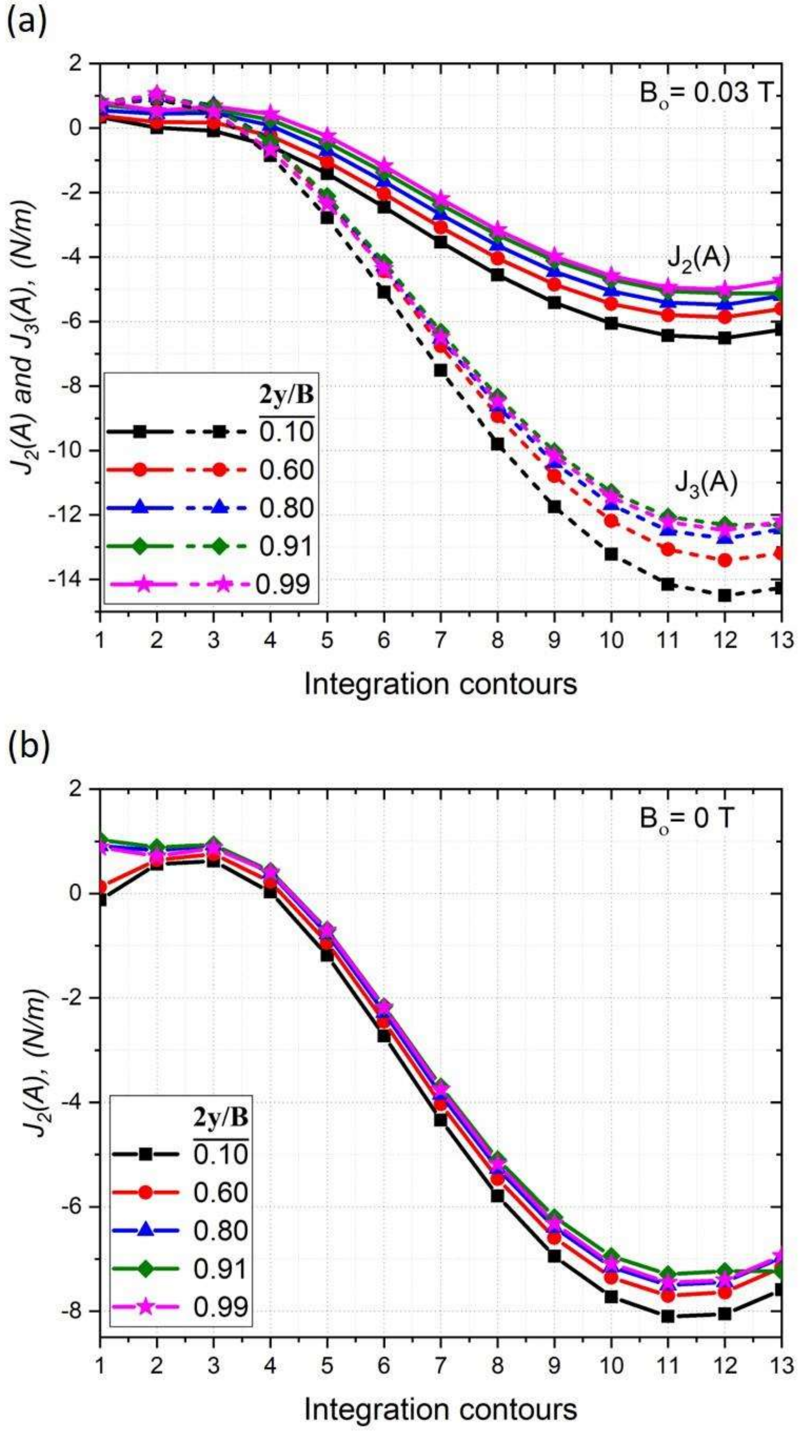

Figure 6.18: Variation of $J_2(A)$ and $J_3(A)$ at different cross-sectional planes under (a) $B_o = 0.03\ T$ and (b) $B_o = 0\ T$

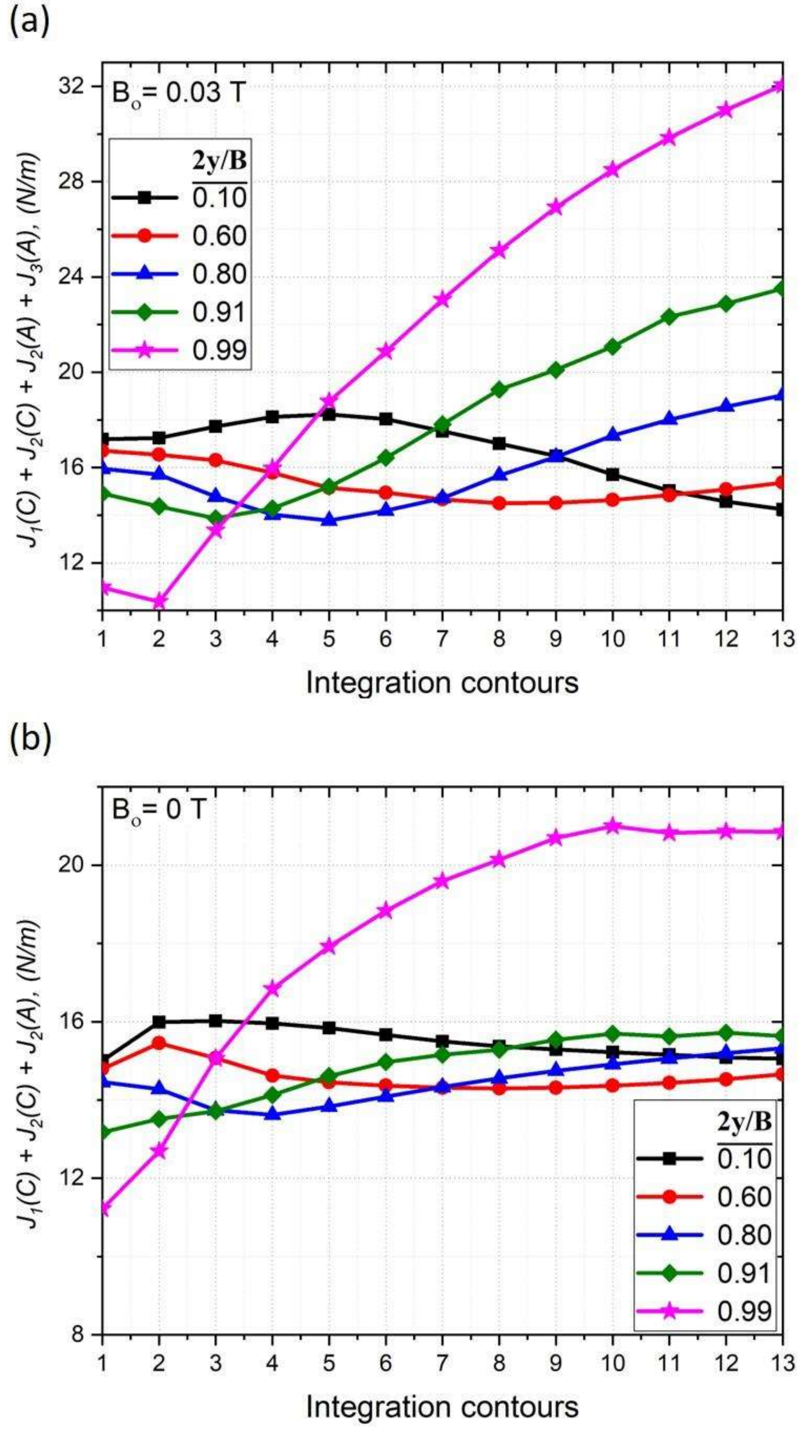

Figure 6.19: Variation of $J_1(C) + J_2(C) + J_2(A) + J_3(A)$ at different cross-sectional planes under (a) $B_o = 0.03$ T and (b) $B_o = 0$ T

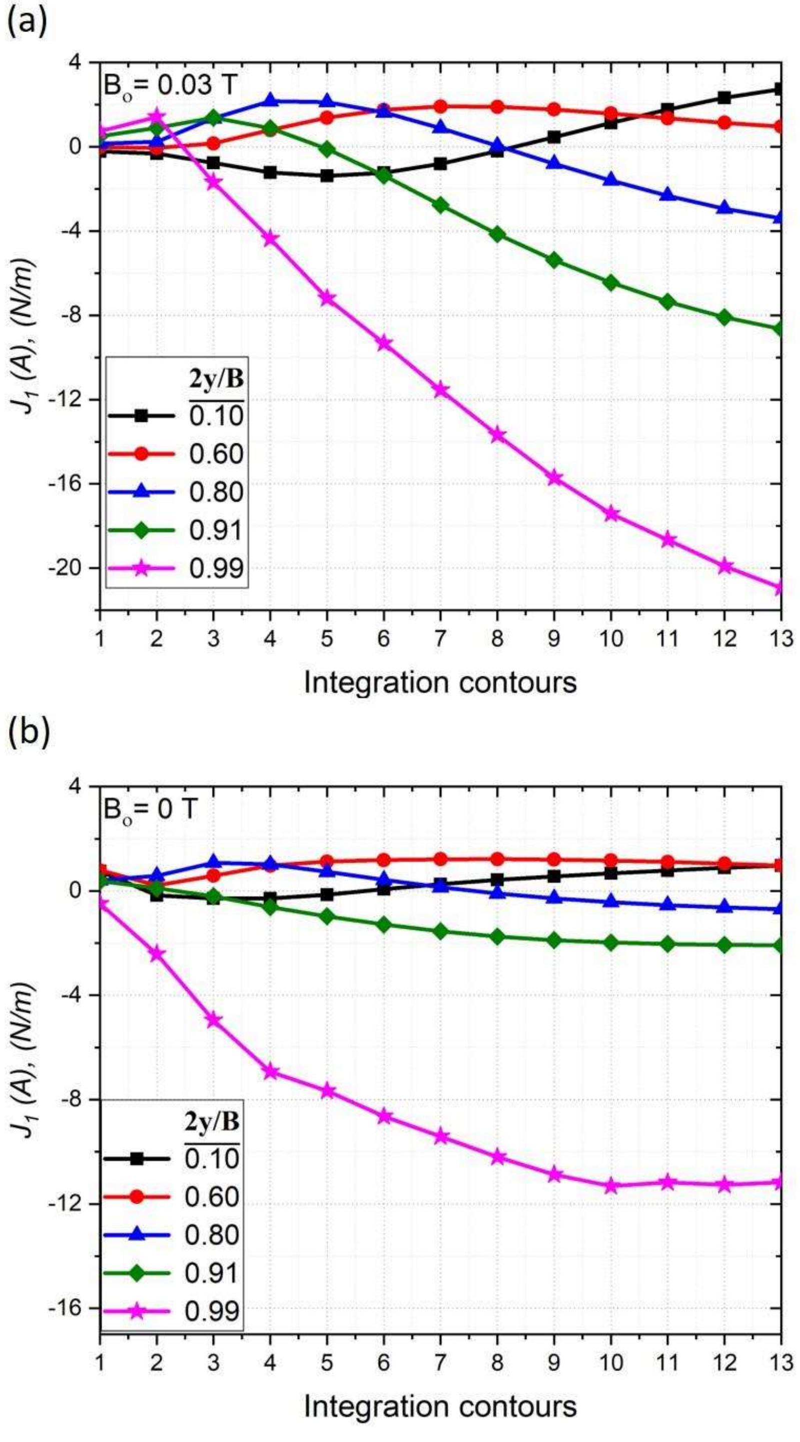

Figure 6.20: Variation of $J_1(A)$ at different cross-sectional planes under (a) $B_o = 0.03\ T$ and (b) $B_o = 0\ T$

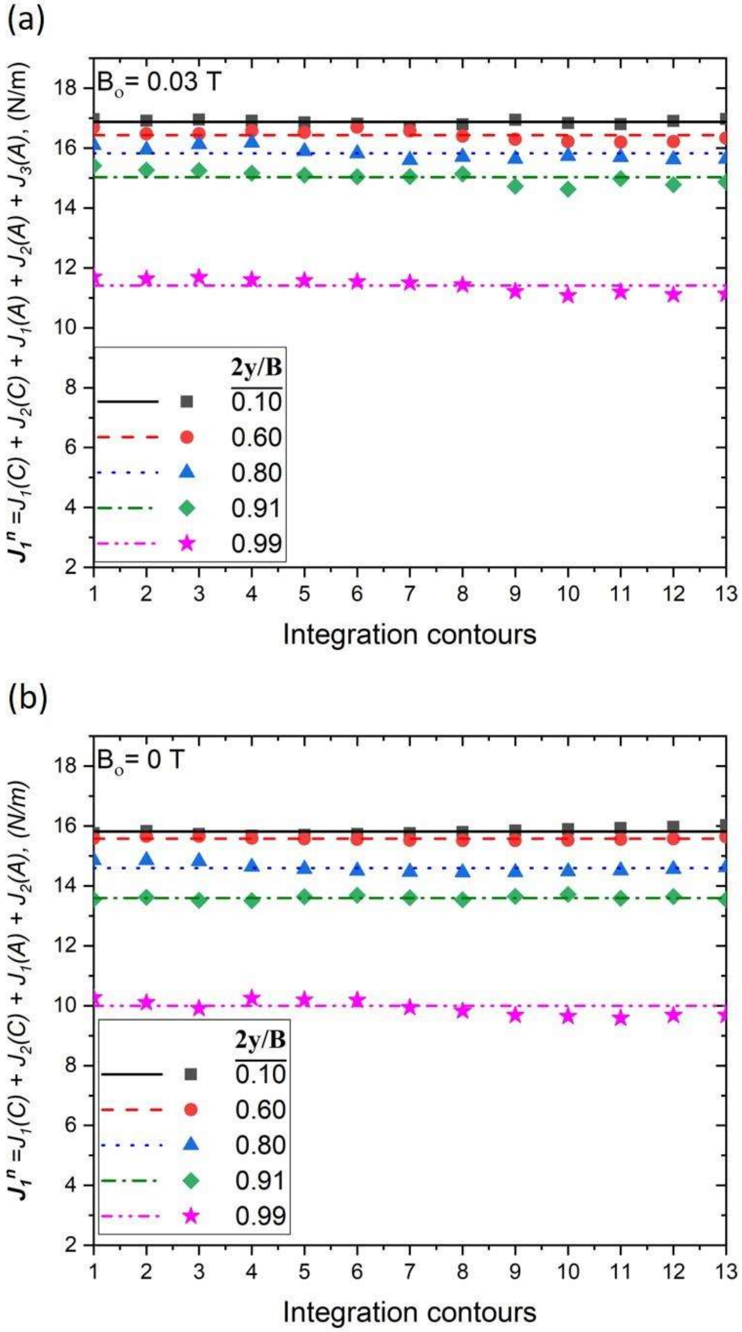

Figure 6.21: Path independence of 3-D J-integral, $\mathrm{J}_1^{\mathrm{n}}$, at different cross-sectional planes under (a) $\mathrm{B_o} = 0.03\ \mathrm{T}$ and (b) $\mathrm{B_o} = 0\ \mathrm{T}$

The values of area integral $J_1(A)$, computed as the gradient of the quantity $\sigma_{i3}u_{i,1}$ over the element in y-direction (or X_3-direction) at each cross-sectional xz-planes, are shown in **Figure 6.20**. Even though $J_1(A)$ changes with x-direction and through thickness locations, it is evidently approaching zero as $x \rightarrow 0$ in each cross-sectional xz-planes. Analogous to the $J_1(C) + J_2(C) + J_2(A) + J_3(A)$ values, the presence of a magnetic field also enhances the variance of area integral $J_1(A)$ terms, especially in the cross-sectional xz-planes closer to the outer free surface. The constituent integral term $J_4(A)$ depends on the inertia effect of the material. Since the loading rate is meagre in the experiment and closely resembles the quasi-static circumstances; hence $J_4(A)$ adheres to the nominal values, that are ignored. When a magnetizable material is subjected to an external magnetic field, it experiences a magnetic body force and can be determined using Eq. (4.18). There is no field gradient since the magnetic field is applied uniformly along the x-direction of the specimen. Hence Eq. (4.18) can be used to conclude that no magnetic body force is acting on the specimen ergo vanishing the $J_5(A)$ integral term.

When all the constituent integrals are included, the excellent degree of path independence is restored as demonstrated in **Figure 6.21**, consequently highlighting the significance of $J_1(A)$ in achieving the path independence of 3-D J-integral, J_1^n, on the distant contours. The distribution of numerically determined 3-D J-integral, J_1^n, across the specimen thickness is depicted in **Figure 6.22**. It is revealed that the J_1^n values due to the three-dimensional effects diminish near the free surfaces. It is also observed that the J_1^n values at the mid-thickness have the largest values because the plane-strain condition is assumed to be predominant. This propensity might explain why the onset of fracture in actual materials occurs near the mid-plane of the specimen's thickness. Therefore, the 3-D J-integral (J_1^n) values at the specimen’s mid-thickness can be termed the critical energy release rate J_{Ic}. In an external magnetic field, the 3-D J-integral (J_1^n) is estimated to be greater. The comparison of the plateau in the 3-D J-integral (J_1^n) distribution near the mid-plane could imply that the plane-strain state is more ascendant in an external magnetic field.

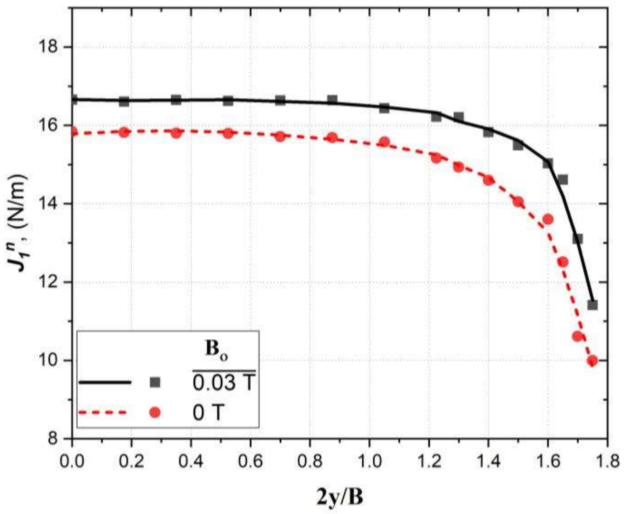

Figure 6.22: Distribution of 3-D J-integral, J_1^n, across the thickness

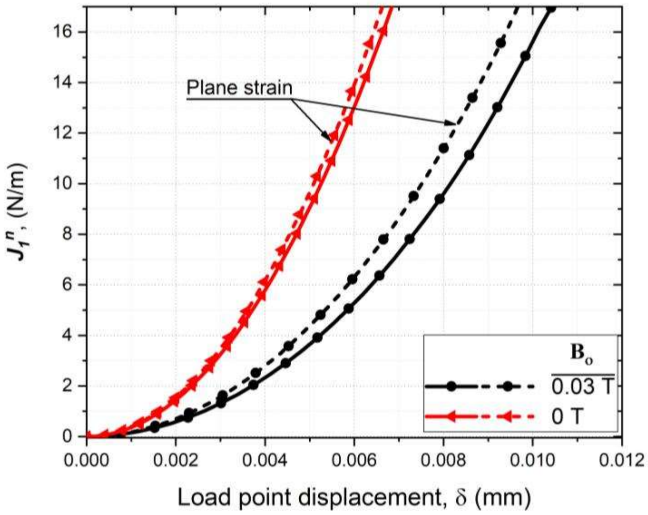

Figure 6.23: 3-D J-integral, J_1^n, at mid-plane vs load point displacement (Solid lines: 3-D J-integral at mid-plane; Dashed line: 2-D plane strain)

The 3-D J-integral (J_1^n) values near the mid-plane varying with load line displacement (δ) is illustrated in **Figure 6.23**. The **Figure** also included the results of the 2-D plane strain simulations. The 3-D J-integral (J_1^n) values in the small deformation regions almost matches the 2-D plane strain J_1-values. In the large deformation regions, the 2-D plane strain J_1-values are found to be greater in comparison to 3-D J-integral (J_1^n) values. It can also be seen that with the application of external magnetic field, the specimen's deformation increases.

Even though a plane-strain state is anticipated adjacent to the crack-front at the mid-plane, for larger deformations the 3-D J-integral (J_1^n) value at the mid-plane does not agree with that predicted from the 2-D plane strain computations. This phenomenon may be due to the fact that, while the plane-strain state is thought to be met near the crack-front at the mid-plane of the finite thick specimen, the actual stress-strain state in the specimen differs from that in an infinite thick specimen. Consequently, the three-dimensional assessment is believed to be essential to a finite-thick SENB specimen subjected to 3-point loading.

Table 6-4: Critical energy release rate (J_{Ic}) values in 3D and 2D non-linear elastic computation.

Contour	$B_o = 0.03\,T$			$B_o = 0\,T$		
	2-D J_{Ic} value (Jin et al. model [54]) (N/m)	2-D J_{Ic} value (N/m)	3-D J_{Ic} value (N/m)	2-D J_{Ic} value (Jin et al. model [54]) (N/m)	2-D J_{Ic} value (N/m)	3-D J_{Ic} value (N/m)
1	51.317	20.432	16.961	18.351	17.332	15.762
2	51.215	20.035	16.918	18.279	17.248	15.825
3	51.129	20.321	16.955	18.193	17.168	15.734
4	51.305	20.108	16.917	18.18	17.151	15.671
5	50.337	19.851	16.855	18.209	17.173	15.699
6	49.445	19.614	16.806	18.232	17.189	15.729
7	48.646	19.450	16.717	18.252	17.202	15.760
8	47.803	19.362	16.789	18.274	17.219	15.802
9	47.053	19.331	16.942	18.297	17.238	15.850
10	46.752	19.334	16.842	18.319	17.257	15.896
11	46.652	19.364	16.802	18.34	17.276	15.936
12	46.553	19.424	16.901	18.359	17.294	15.971
13	46.447	19.472	16.975	18.358	17.295	16.027
Average	48.819	19.700	16.875	18.280	17.234	15.820

The numerically estimated 2-D plane strain and 3-D J-integral (J_{Ic}) values at the mid-plane with corresponding mean values are tabulated in Table 6-4 for each contour in presence and absence of an external magnetic field. In the present work, the framework utilised to evaluate the computational J-integral values was a magnetization and stress dependent elasticity problem with nonlinear properties. Additionally, the phenomenological linearized model (by ignoring $\tanh(x)$ terms) introduced by Jin et al.[54] are used to evaluate the 2-D plane strain (J_{Ic}) values for the comparison purpose and also listed in **Table 6-4**. It is evident from the **Table 6-4** that the linearized model [54] predicts larger 2-D plane strain (J_{Ic}) values than the proposed model [27], and this discrepancy gets more pronounced as the magnetic field increases. This mismatch is explained by the fact that the linearized 3-D model can only accurately characterize the stress-strain curve in the low stress region [27]. The discrepancies are significant at higher stresses and rise with the increasing magnetic field because it considers the nonlinear part of elastic strain to be linear, deviating from the realistic observations. Moreover, the average J-integral (J_{Ic}) values in the magneto-elastic nonlinear stress field listed in Table 6-4 are substantially higher than the experimental values evaluated assuming the linear stress-strain field. Since Terfenol-D inherently possess non-linear characteristics [5,28], therefore such contrasting influence on J-integral (J_{Ic}) values have been observed when comparing effect of the linear and nonlinear constitutive behaviour of material. It is yet to be determined whether the 3D J-integral based on linear or bi-nonlinear is the superior estimator for quantifying the critical fracture parameter. This was further evident from the examination of the experimental J-integral (J_{Ic}) values based on the elastic component of absorbed energy, which is shown in **Figure 6.12** and noted in **Table 6-3** as $17.31\ N/m$ and $15.45\ N/m$ in the presence ($0.03\ T$) and absence of external magnetic field. The average values of critical strain energy release rate (J_{Ic}) in the magneto-elastic bi-nonlinear stress field summarized in Table 6-4 are noted as $16.875\ N/m$ and $15.820\ N/m$

in the presence ($0.03\ T$) and absence of external magnetic field. This demonstrates the adequacy and significance of the nonlinear magneto-elastic 3-D J-integral (J_{Ic}) in the estimation of the fracture parameters for the giant magnetostrictive materials exhibiting magneto-elastically influenced constitutive behaviour. Table 6-3 shows the experimental J-integral (J_{Ic}) values against the peak load corresponding to three-point SENB fracture experimentation. The authors endeavored to identify the root cause of the difference obtained in the experimental J-integral (J_{Ic}) values between the two methods suggested by ASTM. The cause for this is that the technique of computing experimental J-integral (J_{Ic}) based on unimodular (or linear) material model is relies on the peak load, constant elastic modulus and specimen geometry, which cannot account for bi-nonlinearity. The experimental J-integral (J_{Ic}) values based on the elastic component of absorbed energy is determined by evaluating area under the load-displacement curve (i.e., elastic energy) and geometric factors. Observations have shown that the experimental J-integral ($\mathrm{J_{Ic}}$) values based on the elastic component of absorbed energy is closer to the numerical bi-nonlinear 3D J-values and underlying the importance of inclusion of bi-nonlinearity in $\mathrm{J_{Ic}}$ determination. It is worth noting that the magnetic fields have minimal effect on the apparent 3-D J-integral (J_{Ic}) values. In contrast, peak fracture load is influenced by the magnetic fields. The increased energy release rate owing to coupled magneto-elastic phenomena is attributed to the decrease in peak fracture load.

Incorporating magnetization and stress dependent nonlinearity in evaluating fracture parameters increases the computational complexity and necessitates a high-capacity computation facility. Neglecting the giant magnetostrictive material's peculiar properties, such as the nonlinear magneto-elastic response and variability in elastic modulus, may result in the fallacious design of the intelligent devices used in extreme environments, leading to a catastrophe. Hence, it is beneficial to consider the nonlinear magneto-elastic effects in determining the critical energy release rates rather than to get the stress intensity factors from peak fracture load, which has been the standard method for most cases involving fracture-dominant failures.

6.6. Summary

This Chapter primarily concentrates on the influence of the bi-nonlinearity on the characterization of Mode I fracture parameter J_{Ic} for a cracked giant magnetostrictive material in the coupled magneto-elastic field. An experimental study was first conducted to investigate the crack extension behaviour of notched Terfenol-D specimens under three-point flexure loading in the absence and presence of a magnetic field. Terfenol-D fractured at a lower load when an external magnetic field was applied, and the peak fracture load data varied over a wide range due to the material's unknown tensile strength. Then the Weibull statistical theory of strength is utilized to estimate the peak fracture load data. The mean peak fracture load is calculated using the least square technique (LIN2), as well as biased and unbiased maximum likelihood estimation (MLE2-B & MLE2-U). The mean values 54.134 N and 46.616 N obtained from the MLE2-U estimator in the absence and presence of a magnetic field, respectively, are used to calculate the experimental and numerical critical strain energy release rate parameter J_{Ic}. The experimental J_{Ic} value based on the area under the load vs displacement curve of the SENB experiment is determined as 17.31 N/m while applying the magnetic field and 15.45 N/m without the application of external magnetic field. According to ASTM E399, the experimental fracture parameter J_{Ic} is evaluated using the mean fracture load values and constant intrinsic elasticity modulus of Terfenol-D. This results in incorrect fracture parameter J_{Ic} values because this method does not consider the bi-nonlinearity effect. Finally, a finite element study has been conducted to evaluate the three-dimensional path independent J-integral as a critical fracture parameter in a magneto-elastic field. The average values of critical strain energy release rate (J_{Ic}) evaluated as 16.875

N/m and 15.820 N/m in the presence (0.03 T) and absence of external magnetic field, respectively, which is closer to the experimental J_{Ic} values (evaluated from load-displacement curves). This validates the appropriateness of the proposed bi-nonlinear constitutive magneto-elastic model. For the bi-nonlinear stress-strain field in the magneto-elastic domain, the 2-D and 3-D J-integrals are assessed on thirteen distinct contours. The model's legitimacy and usefulness are demonstrated by the outstanding degree of path independence of all contours. Because of bi-nonlinearity, the 2-D plane strain J-integral and 3-D J-integral values diverge significantly from the experimental fracture parameter J_{Ic}. Because the plane-strain condition is expected to be prevailing, the 3-D J integral values are bigger at the specimen's mid-plane than at the free surfaces. In an external magnetic field, the 3-D J-integral is estimated to be greater owing to more ascendant plane-strain state. It is also noticed that the 2-D plane strain J-integral values are substantially different from the 3-D J-integral values owing to the three-dimensional effects. This difference increases with the application of external magnetic field as for the larger deformations the actual stress-strain state in the finite specimen considerably differs from that in an assumed infinite thick specimen. Thus, the three-dimensional assessment is believed to be essential to a finite-thick SENB specimen. Hence, it is beneficial to consider the nonlinear magneto-elastic effects in determining the 3-D critical energy release rates (J_{Ic}) rather than to get the J_{Ic} from the peak fracture load, which has been the standard method for most cases involving fracture-dominant failures.

This Page is Intentionally Left Blank